UNIVERSITY OF OKLAHOMA

GRADUATE COLLEGE

A NEW FRONT-END SYSTEM FOR UAV-BASED ANTENNA MEASUREMENTS FOR POLARIMETRIC WEATHER RADARS

A THESIS

SUBMITTED TO THE GRADUATE FACULTY

in partial fulfillment of the requirements for the

Degree of

MASTER OF SCIENCE

By

KHUDA BURDI

Norman, Oklahoma

2023

A NEW FRONT-END SYSTEM FOR UAV-BASED ANTENNA MEASUREMENTS
FOR POLARIMETRIC WEATHER RADARS

A THESIS APPROVED FOR THE
SCHOOL OF ELECTRICAL AND COMPUTER ENGINEERING

BY THE COMMITTEE CONSISTING OF

Dr. Jorge L. Salazar-Cerreno, Chair

Dr. Caleb Fulton

Dr. Yan Zhang

Acknowledgments

I would like to express my heartfelt gratitude to my parents, Abuzar Ali and Bibi Numa, for their unwavering support and the values they have instilled in me. Their constant encouragement and strength have been a guiding force throughout my journey, and I am truly grateful for their unwavering support. I would also like to acknowledge my siblings for their selfless support and presence in my life.

I extend my deepest appreciation to Dr. Jorge Salazar-Cerreno, my advisory chair, for his exceptional support and mentorship during my research journey. His guidance and encouragement have played a pivotal role in shaping me into a better engineer, and I am sincerely thankful for his unwavering dedication to my success. Additionally, I would like to express my sincere gratitude to Dr. Caleb Fulton and Dr. Yan Zhang, the other members of my committee, for their expertise and valuable insights. Their contributions have significantly enriched my experience at the University of Oklahoma.

I am immensely grateful to Dr. Antonio Segales for his consistent support throughout my research. His guidance and encouragement have been invaluable assets on this journey. I would also like to extend my appreciation to Ms. Elizabeth Joyce for her assistance and unwavering presence. I want to express my heartfelt thanks to my dear team, PAARD, for their constant encouragement and selfless contributions to my research. Their dedication and support have been vital in the realization of this project.

Finally, I would like to extend my sincere gratitude to the Advanced Radar Research Center (ARRC) for their research support and the National Oceanic and Atmospheric Ad-

ministration (NOAA) for their generous financial support of this project. I am truly grateful for the opportunity to collaborate with ARRC and NOAA, and I deeply appreciate their commitment to advancing scientific exploration and innovation in the field of radar technology. Their sponsorship has played a crucial role in the successful completion of this project, and I am honored to have been a part of this partnership.

Abstract

Radar system calibration is vital for ensuring optimal performance, especially in weather radars that have stringent requirements for co-polarization mismatch. In-field calibration is essential, particularly for mobile weather radars, as environmental conditions can vary between deployments. Traditionally, conventional far-field ranges or airborne systems such as helicopters and aircraft have been used to measure and calibrate radar systems. However, in recent years, Unmanned Aerial Systems (UAS) have emerged as a cost-effective and flexible alternative for antenna measurement and radar calibration.

Previous studies have demonstrated the feasibility of using UAS for far-field antenna measurements across various operating frequencies. These works have achieved high accuracy in characterizing and calibrating polarimetric weather radar systems, meeting critical requirements such as co-polarization mismatch below 0.1 dB and cross-polarization isolation below -45 dB. However, existing UAS-based systems are complex to operate, requiring multiple equipment both on the UAS and the ground station. They are primarily limited to one-way transmission from the UAS to the AUT and lack the capability to switch between RX and TX measurements or H- and V-polarization without physical modifications.

The objective of this thesis is to develop a lightweight and self-contained front-end system for UAS-based in-situ antenna characterization. This system will eliminate the need for additional RF instruments on the ground, providing remote real-time control to switch between RX and TX modes in both V- and H-polarization. It will also facilitate the transmission and reception of measurement data over long distances, enabling far-field

measurements beyond 120 m.

The proposed system aims to address the limitations of existing UAS-based calibration systems, offering a sophisticated and accurate solution for measuring the strictest radar systems. By developing a versatile and lightweight front-end system, this research seeks to advance the field of UAS-based antenna characterization and contribute to the improvement of radar calibration techniques.

Table of Contents

List of Figures

Chapter 1

Introduction

1.1 Motivation

There has been a push to transition from traditional dish-based and mechanically steered weather radar systems to fully digital dual-polarized phased array weather radar systems with electronic scanning capabilities in recent years. Phased array radar have become ideal for weather surveillance due to their fast scanning updates, reconfigurability, adaptability, scalability, and relatively lower long-term costs [1]. However, these systems face challenges due to the inherent dependence of phased arrays' radiation characteristics on scan angle, unlike mechanically steered dish-based systems. To ensure accurate performance and avoid errors in polarimetric weather radar products, precise characterization and calibration of the radar is required [2, 3]. The process of characterizing antennas requires specialized indoor or outdoor range facilities, such as anechoic chambers and open wide spaces free of reflective objects, that provide the necessary RF instrumentation, technical procedures, and physical space for accurate measurements [4, 5]. While testing in an anechoic chamber is the first step, antennas characterized in controlled indoor conditions may not perform identically in outdoor environments under normal operating conditions. Various environmental factors such as temperature, humidity, weather conditions, ground clutter, RF interference, and component failure rate can significantly impact the radiation

characteristics and overall performance of an antenna [6]. Therefore, outdoor in-situ range facilities are essential to measure the antenna system's performance in its final installation site and predict its interaction with the environment [7]. However, developing large outdoor range facilities for static radars can be expensive and impractical. There are solutions that minimize the need for outdoor infrastructure such as calibration with a tower but they also have limitations [8]. This challenge has led to the exploration of alternative methods and equipment for mobile in-situ antenna measurements that do not require expensive and low usage facilities. Tethered balloons and helicopters have been used in the past to perform airborne measurements of large antennas [9, 10, 11], providing advantages in terms of cost constraints and the ability to deploy antenna test and evaluation solutions across multiple sites. These measurements involve mounting a probe antenna on an airborne manned air-crafts.

The advancement of unmanned aerial systems (UAS) has opened up new possibilities for cost-effective in-situ antenna characterization [10, 11, 12, 13, 14]. UAS combine commercially available aircraft, off-the-shelf components, instruments, and sensors to create customized solutions for specific scientific requirements [15, 16, 17, 18]. UAS-based antenna measurement system offer flexibility and portability, allowing measurements to be performed without extensive modifications to the test site [6]. However, there are still uncertainties surrounding the impact of environmental factors, flight strategies, and UAS stability on measurements, especially for polarimetric phased array weather radars that require precise co- and cross-polarization antenna patterns. Additionally, the presence of the UAV structure introduces scattering and diffraction effects that can degrade the radiation characteristics of the probe antenna, affecting co-polarization matching and cross-polarization levels [19].

Previous efforts in UAS-based antenna measurements have primarily focused on the VHF and UHF ranges of the RF spectrum. However, characterizing weather radars us-

ing UAS presents unique challenges due to the criticality of stability, misalignment errors, and aiming accuracy in microwave frequencies. Achieving centimetric precision is crucial for accurate measurements. Fortunately, advancements in UAS technology have improved aerial stability through gyroscopic stabilization, inertial measurement units, and autonomous flight modes. Flight controllers and Real Time Kinematics (RTK) algorithms have significantly enhanced UAS positioning accuracy, reducing errors from meters to centimeters. Furthermore, adaptive controllers for multi-rotors on the system enable development of stable platforms that can perform even in high wind conditions, while advancements in batteries and motors technology have extended flight duration considerably [6, 19]. There have been some successful implementations of UAS-based antenna characterization, such as using metal spheres tethered to balloons as calibration targets, achieving a standard deviation of 0.1 dB remains a desired target for accuracy [6]. Current implementations have shown values as low as 0.2 dB in passive UAS-based characterization using metal spheres tethered to such systems. However, recent active UAS-based antenna characterization have received the 0.1 dB desired target in certain UAS configurations. One recent notable implementation involved a UAS-mounted probe for both co-polarization and cross-polarization characterization of an antenna. The study involved simulations, calculations, and the development of a framework for antenna and radar characterization. However, this implementation was limited to the transmitter (TX) being on the UAS while the receiver (RX) remained on the ground [19].

1.2 Literature Review

The field of in-situ antenna radiation pattern measurements has seen significant developments over the years. In the mid-1960s, Steele [9] introduced the concept using a tethered balloon with a dipole as a probe antenna, successfully obtaining partial elevation

gain patterns while the Antenna Under Test (AUT) was rotating. However, the inability to accurately control the position of tethered balloons posed significant challenges and limitations. Decades later, in the late 1980s, Lejerkrans and Manton [10, 11] introduced a helicopter-borne measurement method capable of operating in HF up to S-band ranges. This method involved mounting a wide-beam probe antenna under the aircraft and recording field strength measurements transmitted by the AUT as the helicopter flew in different paths. The use of manned aircraft allowed for high precision measurements, but the approach was expensive, unsustainable and impractical.

In recent years, there has been rapid progress in RF measurement and characterization using unmanned aerial system of various sizes. The availability of commercial off-the-shelf flight solutions with high precision and performance at lower costs has significantly contributed to such advancements. These UAS are equipped with GNSS such as GPS, inertial measurement units (IMU), radio frequency equipment such as a field strength measurement system, and at least one antenna dedicated as a probe. Most research efforts have focused on radio astronomy applications in the VHF bands, but there is an increasing demand for accurate antenna radiation pattern characterization in microwave telecommunication systems [16], especially with the emergence and implementation of 5G technologies. Examples include hexacopter systems for large aperture array measurements and compact, low-cost system for S and C bands characterizations. While co-polarization radiation patterns have been extensively studied due to the higher radiation power and relative resistance to contamination from ground reflections and multi path, the characterization of cross-polarization patterns and polarimetric systems remains an open area of research. Previous works have provided insights into UAS-based antenna measurements and calibration for polarimetric weather radars, as well as methods for obtaining antenna and radar constants using metallic spheres and UAS.

One of the best implementations of such a system was achieved in 2020 [19]. In this

implementation, a custom probe was been designed and fabricated specifically for application in UAS based polarimetric antenna measurements in S-band. It should be noted that this system only had the TX component onboard the UAS alongside an additional custom switching polarization circuitry. This circuitry allowed for the transmission of continuous wave (CW) signals in both orthogonal polarization by rapidly switching between them at very high speed. This enabled the measurement in both polarization during the same flight mission, resulting in a twofold improvement in measurement time, although at the expense of additional signal post-processing. It's worth noting that the system did not offer the capability to transmit in one polarization at a time without hardware modifications. The transmitter, which utilized a synthesizer, was designed to be lightweight and capable of transmitting up to 20 dBm without the need for an amplifier circuit. Nevertheless, it was primarily designed to operate exclusively in continuous wave mode at the desired frequency. The RF system onboard the UAS was intentionally kept simple and bare-bone since most of the processing and data collection occurred at the ground station, which was bulkier in comparison to the airborne counterpart. On the receiver (RX) end, a handheld microwave analyzer, Field Fox N9917A, along with an external amplifier board consisting of low-noise amplifiers (LNA) and power amplifiers (PA), was used. The Field Fox N9917A served as a portable high-performance RF and microwave analyzer, providing precision akin to a bench-top system. However, it's important to mention that this system lacked the capability to switch TX and RX from the UAV or switch between horizontal and vertical polarization in real-time based on user input [19].

1.3 Proposed Work

In the proposed research, a custom lightweight RF system will be developed using a software-defined radio (SDR) to be deployed on a custom UAS platform. An accompanying amplifier circuit to support the internal gain of the SDR on both RX and TX channels will also be implemented. The system will also include a low noise, high isolation, electromechanical RF switch to enable seamless switching between orthogonal polarization for either RX or TX. The integration of the system with the UAS will establish a fast and stable communication between all components.

The RX channel of the SDR will capture In-phase and Quadrature (IQ) data from the onboard probe through the low-noise amplifier circuit. The IQ data will then be processed on the onboard computer to calculate the received power value in dBm. The high-resolution power value will be transmitted to the Pixhawk, the main flight controller on the UAS. The UAS will have the capacity to store high-quality data onboard the Pixhawk, while simultaneously transmitting real-time data to the ground station for monitoring. It is important to note that the ground station's main purpose is to ensure monitor communication and safe operation of the UAS but its use with the RF system is optional and limited to real-time monitoring purposes.

To facilitate communication between the UAS and the ground station, a modified version of the open-source Mavlink protocol will be used. The UAS will read power data from the SDR and transmit it to the ground station using a custom message built by the onboard computer and relayed through Mavlink Proxy and the primary UAS 915 MHz telemetry hardware. This real-time data transmission will enable researchers to monitor and analyze the measurements during operation, allowing them to make necessary adjustments and modifications on the fly. The Mavlink protocol serves as an effective and standardized means of seamless and efficient information exchange regarding the operation, safety, and

health of the UAS.

On the TX end, the onboard computer will generate custom continuous and pulse waveform based on the specific application and measurement. These waveform will be generated at one of the SDR TX ports. Depending on the selected orthogonal polarization, the transmitted signals will pass through the power amplifier circuit and be transmitted via the probe antenna. Full control over the RF system, including switching between RX or TX modes and selecting the polarization (horizontal or vertical), will be available from the UAS radio controller. This control mechanism will provide operators with the flexibility to adjust and operate the RF system according to the experiment or mission's specific requirements.

1.3.1 Contribution

The primary contribution of this research is the development of a completely new RF front-end system for a UAS-based antenna characterization system, specifically designed for the characterization and calibration validation of radar systems, including sophisticated static and mobile polarimetric weather radars. The new front-end system is self-contained and capable of both transmitting and receiving signals in H- and V-polarization without the need for additional RF components or ground-based processing during airborne operations. Moreover, it can also be easily utilized on the ground (AUT) with minimal or no modifications.

The key features of the new front-end system are as follows:

- Lightweight and self-contained design.
- Real-time remote switching between RX and TX modes in both H- and V-polarization.
- Capability to store or transmit RX data from either polarization over long distances in real time.

- Compatibility with both UAS-mounted operations and ground-based AUT scenarios.
- Utilization of a wide-band probe for operation in 2 GHz - 18 GHz frequency range.
- Integration of custom MATLAB-based GUI interfaces for real-time measurement and processing of power data.
- Provision of guidelines encompassing instrumentation, procedures, best practices, and limitations of the proposed system.

The significant contribution lies in the transition from a single high-power synthesizer to a software-defined radio capable of performing both transmission and reception tasks. A newer and lighter amplifier circuit design is presented that allows for the addition of external gain to the internal gain of the SDR, with total RX gain of up to 80 dB. The power output of the system is increased up to 30 dBm, which is more than the 20 dBm output of the previous relevant design, this also comes with reduction in weight which is crucial for SWaP in UAS applications. The SDR provides excellent control over all integrated RF components, enabling real-time switching between RX and TX modes during flight, as well as polarization switching. Depending on the UAS configuration for the flight, we can perform simultaneous V and H transmission or reception to measure or transmit in co-polarization and cross-polarization, respectively.

1.4 Thesis Outline

The paper presents a comprehensive study on the design and evaluation of a new RF system for unmanned aerial system for antenna characterization in 5 chapters. Chapter 2 is a detailed discussion of the design aspects of the UAS, highlighting the gimbal mechanism, positioning, and the integration with the RF system for real-time transmission of power data to the ground. The RF sub-system design is thoroughly discussed, with specific

attention given to the RX system, RX channel isolation for simultaneous co-polarization and cross-polarization measurements, the TX system, RF switch, and the two different probes under study. Chapter 3 discusses the experimental setup, which includes the radiation frequency of operation, the antenna under test, and the different modes of operation. This chapter details the chamber test, where measurements are conducted with the new RF system both with and without the UAS. These measurements are then repeated in an outdoor environment under identical conditions. Finally, a flight test is conducted to obtain field results, assessing the UAS performance in real-world scenarios. In Chapter 4, the results from the experiments presented in Chapter 3 are provided and discussed in detail. The analysis includes comparisons between measurements conducted inside the chamber and those performed in an outdoor setting. The impact of the UAS on the antenna characterization process is evaluated, considering factors such as accuracy, signal quality, and performance stability. The findings provide insights into the effectiveness and reliability of the UAS-based antenna characterization system. Chapter 5 serves as the conclusion of the paper, summarizing the key findings and contributions. It highlights the successful design and implementation of the UAS for antenna characterization. The results obtained from the experiments validate the system's capability to accurately characterize antennas in both controlled and real-world environments. The thesis concludes by discussing the implications of the research, potential areas for future improvement, and the overall significance of the developed UAS for antenna characterization applications.

Chapter 2

UAS System Design

The context of application and evolution of UAS platform in the field of antenna radiation pattern measurements is discussed in Chapter 1, including a discussion of the shortcomings of each platform evolution and the improvements from updates or upgrades to better platforms. In this chapter, the design of the proposed RF front-end system for antenna patterns measurement and the selection of an efficient and reliable UAS platform for the system will be discussed. The design of the UAS will be addressed first and the design decisions around the platform, the gimbal, positioning and the RF sub-system justified. A detailed design analysis of the new RF subsystem, alonge with the SDR components and operation, the electro-mechanical RF switch system, the IQ data processing and the integration of the RF system with the UAS and the ground station through real-time data monitoring will be highlighted. An analysis of the system integration and design trade offs, with the end goal of creating a system best suited for field in-situ operations and measurements will also be addressed.

The design of the whole system is as illustrated in Fig. 2.1. The hardware mounted on the UAS consists of a probe, the InfinityMR PRO V2 gimbal, RF switch, an external amplifier and filter circuit, a SDR, an onboard computer and a PixHawk CubeOrange. The ground station consists of the D-GPS ground station, a laptop computer with MATLAB or LabView, a telemetry radio and the UAS radio controller. The specifications of these

devices and their roles in the overall systems are explored in the sections ahead.

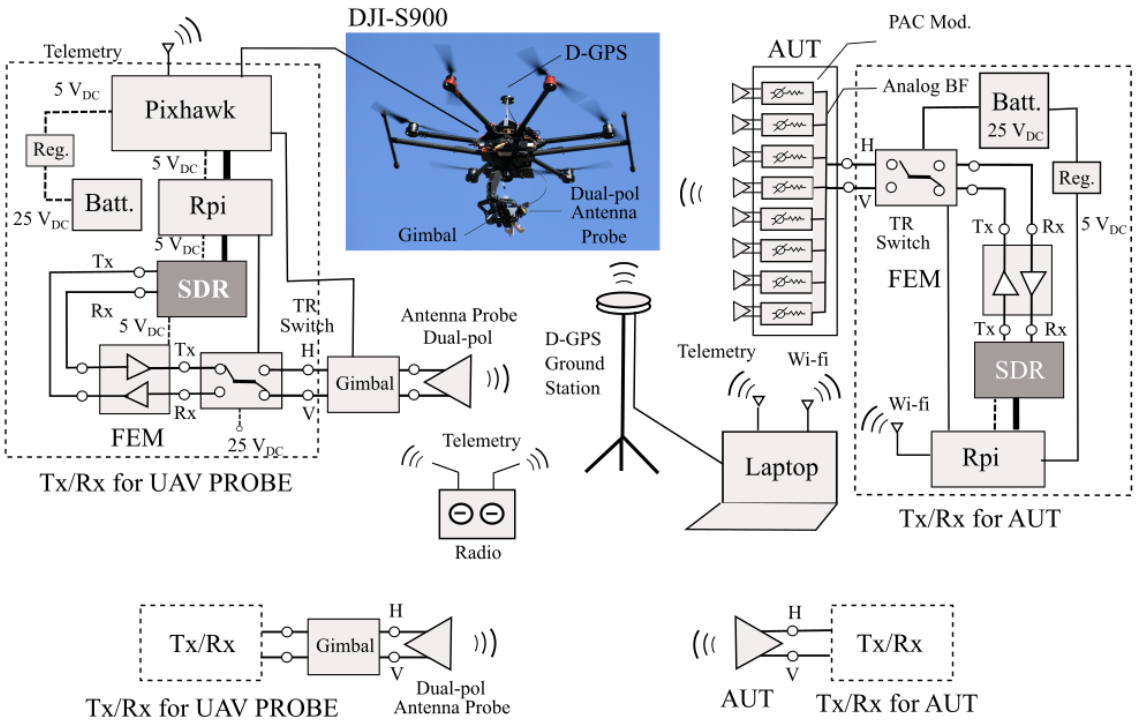

Figure 2.1: Complete block diagram of the UAS and RF subsystem. The left block shows the components as mounted on the UAS with the signal passing from the probe to an RF switch through the gimbal, the onto an external filter and amplifier circuit before reaching the SDR. The SDR and the Raspberry Pi process the IQ data into power and transfer to the Pixhawk which then transmits it to the ground station. This system is further discussed in the next section and Fig. 2.4. For TX, the SDR generates the waveform which pass through the power amplifier circuit and the RF switch before transmission from the probe.

2.1 UAS Platform Design

The proposed UAS is based on the DJI Spreading Wings S900 platform which is a stable and tested platform for antenna and radar measurement applications [19, 20]. The S900 is a hexacopter with an arm-span of 0.9 m and take-off mass of approximately 4 kg without payload. The flight time is dependent on the payload and battery capacity, which for the current system with a payload of 1.2 Kg and a 16000 mAH battery is approximately

20-25 minutes. Depending on the flight mission plan (discussed in Chapter 3), the system can endure up to 5 consecutive co- and cross-polarization measurements per flight before needing a battery recharge. The system has a retractable landing gears, which automatically fold up during takeoff, tucking them out of the way of any payload or probe mounted on a Infinity MR Pro v2 gimbal with a mounting mass of just 0.88 Kg and maximum payload of up to 1.3 Kg, as shown in Fig. 4.3 (a). The gimbal has native Mavlink support and a 360 ° rotation in yaw, making it ideal for tracking targets on the ground. The UAS is running a custom firmware based on the latest Copter version of Ardupilot, an open source software development program for all kinds of UAS and RC applications. Ardupilot is supported by professionals as well as enthusiasts and is one of the most reputable and reliable open-source UAS platforms. The custom firmware is used under the terms of the General Public License (GPL) and is running on a CubeOrange flight controller, developed by Pixhawk as an accessible and reliable high-end controller for UAS and RC applications.

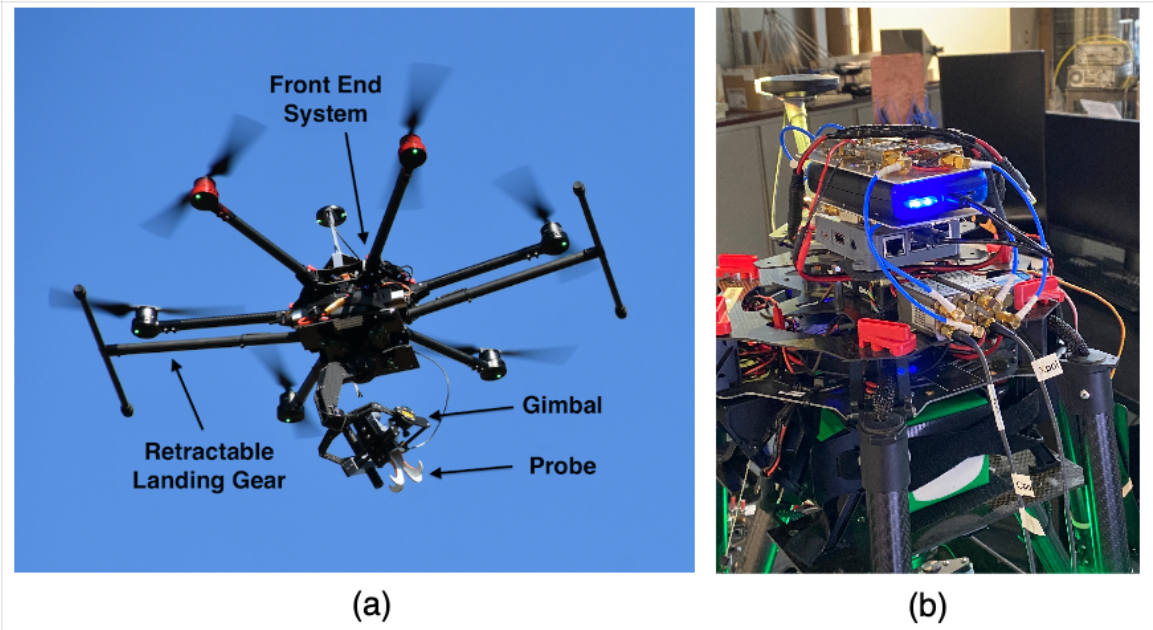

Figure 2.2: (a) The DJI Spreading Wings S900 platform with the InfinityMR PRO v2 gimbal and the wide band open boundary quad ridged horn probe antenna on a custom mount, during flight with retracted landing gears. (b) The new RF Font End system mounted and integrated on the UAS in its final configuration with two RF switches and simultaneous co- and cross-polar measurements.

The versatility of Ardupilot enables several novel and essential features including AUT tracking, custom flight patterns, interfacing with auxiliary onboard computers, 200 Hz onboard data storage as well as 50 Hz real-time data stream over Mavlink to the ground station, which is an essential integration to the system as shown in Fig. 2.1. The telemetry uses a 915 MHz, ultra long range radio with a range of over 4km to transmit UAS status and custom messages through MavProxy using a Raspberry Pi 3 as an external onboard computer. The ground station receives the Mavlink message over MavProxy, including the received power, and plots the RX power using a custom application in MATLAB in real-time. The internal GPS is assisted by a SWIFT-RTK deferential GPS system for cm precision positioning (discussed further in the next section). The PPK location of the AUT and D-GPS reference is recorded using an EMLID PPK tool, which is later processed with

data from the Oklahoma City GPS Center to find the precise GPS location of the AUT and D-GPS reference.

The flight control for the UAS is primarily through the radio controller, a physical handheld controller connected directly and in constant communication with the UAS at all time, while the configuration control is through Mission Planner, a software installed on the ground station computer, also connected directly to the UAS and receiving real-time data to monitor the configuration and health of the UAS. The flight mission plan, number of flights, frequency and AUT position are generated with a MATLAB script and flashed onto the UAS through Mission Planner, while the AUT configuration for the gimbal, waypoint verification and RTK configuration are done directly within Mission Planner. Since controls for the RF subsystem are also integrated into the UAS platform, dedicated switches on the radio controller can be assigned to control features of the RF subsystem in flight, such as switching between RX and TX more or H- and V- polarization. The integration is versatile and additional settings or configurations can be added to the system as long as programmed correctly to the firmware and supported by the RF subsystem.

2.2 Gimbal System

As discussed in Chapter 1, the InfinityMR PRO V2 has been used in previous implementations of UAS based antenna pattern measurements but for this study the gimbal system is running a completely custom firmware and operation modes, based on novel mathematical modeling for an GNSS based AUT tracking [20]. The PRO V2 is a 3-axis gimbal with completely free 360 ° yaw, as shown in Fig. 2.3(b) [21]. Using precise differential GPS coordinates of the AUT and the RTK position of the UAS, the gimbal is able to track the AUT on the ground during flight and keep the probe aligned with the AUT regardless of flight mission plan. Ensuring the probe is always aligned with the AUT during flight

in both the H- and V-polarization, which is essential for any attempt at simultaneous co- and cross-polarization measurements. A 5 mW laser is mounted on the gimbal to monitor the alignment of the probe and track the precision of the gimbal with respect to the AUT, as shown in Fig. 2.3(a) [22].

The probe mounted on the UAS in the initial design was a commercial 2 GHz - 30 GHz, wide-band open boundary quad-ridged horn antenna. The probe was selected based on form factor, weight distribution, size and frequency bandwidth. However, the performance did not meet the -40 dB cross-polarization isolation requirement and was substituted by a custom S-band dual-polarized truncated 4x4 microstrip patch antenna array at 3 GHz with a consistent cross-polarization isolation of under -40 dB (discussed in the next section.)

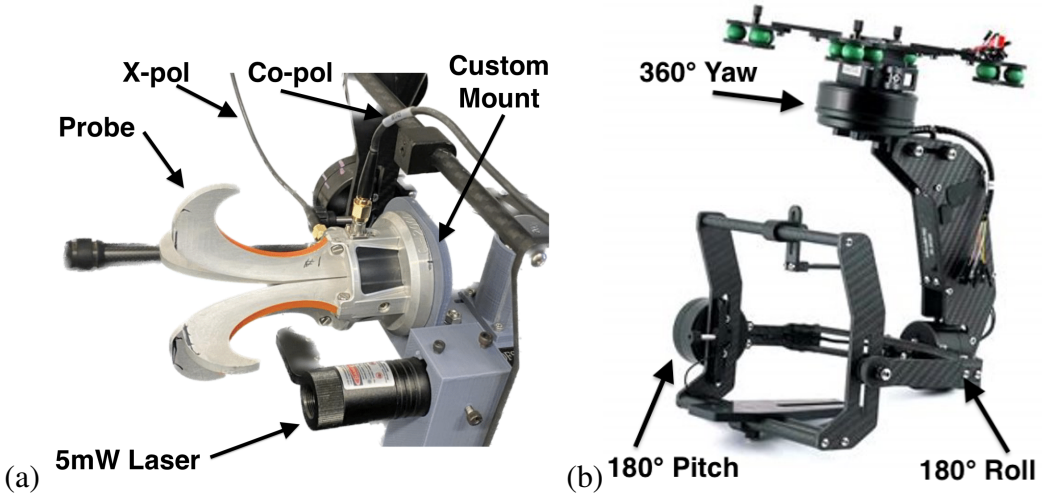

Figure 2.3: (a) A wide band open boundary quad ridged horn probe antenna mounted on an InfinityMR PRO v2 gimbal with a custom mount and (b) InfinityMR PRO v2 gimbal as mounted on the UAS without a probe.

2.3 UAS Positioning

The system relies on a SWIFT D-RTK unit for precise positioning to correct the internal GPS, which is critical for accurate tracking of the AUT by the PRO V2 gimbal.

Consequently, it becomes essential to characterize the precision and accuracy of the GPS positioning of the UAS with and without the RTK-GPS corrections.

Positioning characterization was performed using the most common method of measurements the system while grounded and airborne. During the ground test, the performance was evaluated by simultaneously recording the GPS and RTK positions for a specific duration required for GPS lock, set at 5 minutes for this study. This process was replicated at four distinct locations to identify any potential performance disparities between the internal GPS and RTK-GPS.

The analysis showed that the internal GPS standalone position has variations of up to 26 cm in the horizontal axis and over 56 cm in the vertical axis. These values fall within the specifications provided in the unit's datasheet and align with aggregate mission results. In contrast and expectedly, the RTK assisted GPS position displayed significantly better precision, with variations as little as 0.31 cm in the horizontal axis and 0.66 cm in the vertical axis.

The airborne test involved hovering the UAS at a fixed position and height for the specified duration or until GPS fixed status is achieved. First using the internal GPS standalone and then with RTK corrections, at four different positions similar to the grounded tests. The results showed that the internal GPS position showed variations of up to 26.3 cm in the horizontal axis and over 27.9 cm in the vertical axis, once again following the unit's datasheet specifications and corroborating with aggregate mission results. In contrast, the RTK position demonstrated exceptional accuracy, with variations as minimal as 20.82 cm in the horizontal axis and 10.38 cm in the vertical axis, surpassing the datasheet 25 cm specification and well within the required values for our design.

These results validate that GPS with RTK corrections significantly outperform the internal GPS as a standalone system, making it an optimal choice for the UAS system, especially considering the gimbal performance reliance on precise tracking of the AUT.

2.4 RF-subsystem Design

Starting with components, custom design hardware are the way to go which eliminate features and devices that are not essential to the design of the system. However, the scope of this study is to redesign the font end system resourcefully using off the shelve components. It is ideal to use components that can perform multiple functions and can be shared between the RX and TX, instead of dedicated devices like in the previous design, which adds to the complexity and SWaP.

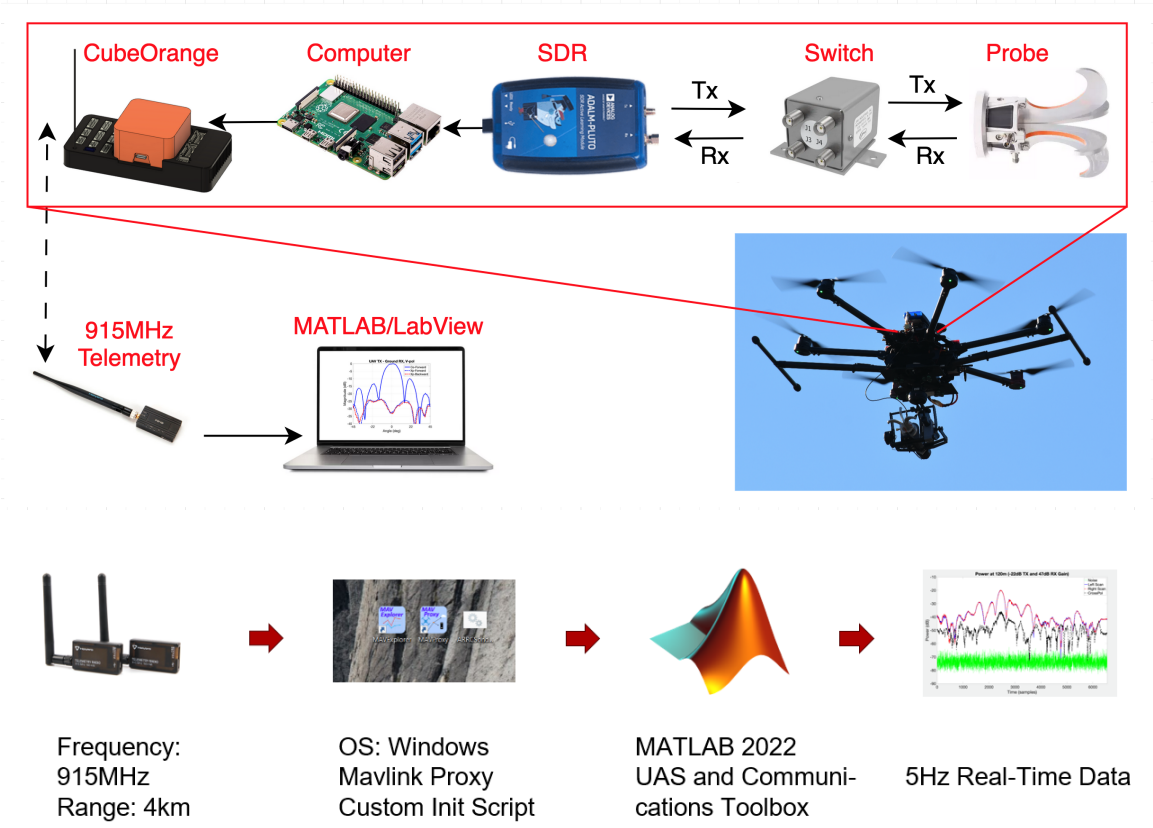

Figure 2.4: The RX-mode RF sub-system block diagram. The power is received as illustrated by the arrows, starting with the IQ data at the probe, passing through the RF-switch before reception at the RX port on the SDR. After processing the IQ data from the SDR, the onboard computer sends the power value to the CubOrange to be stored and transmitted to the ground station through the 915 MHz telemetry. A computer at the ground station receives the telemetry data to output the radiation pattern in real time at 50 Hz.

For such a design, recent advancement in SDR technologies have enabled very efficient and compact SDRs, some integrated with advanced modern transceivers like at the ad9364 from Analog Devices. SDRs are generally not only inexpensive but also extremely versatile as they come integrated with an array of components like FPGAs, analog-to-digital converters (ADC), digital-to-analog (DAC) and onboard flash storage. Since transceivers enable functions of both a transmitter and receiver, SDRs, along with complete internal amplifiers and filters can be used for a magnitude of RF measurements which eliminate redundant components. As such, it also integrates the RX and TX system together, saving a lot of space and weight.

The Adlam Pluto SDR, shown in Fig. 2.5(a), an inexpensive SDR with several internal filters and amplifiers circuit, is shown in Fig. 2.5 (b). The SDR is a low cost and lightweight devices that comes with both an ad9363 and ad9364 version, with a preinstalled firmware for the ad9363. The ad9363 is ideal for single channel RX and TX from 300 MHz to 3.3 GHz at a higher sampling rate of over 60 MHz but minor firmware upgrades enable the full utilization of the ad9364. The ad9364 extends the frequency range up to 6 GHz at lower sampling rate of about 30 MHz over dual channel TX and RX, for a total of 4 independent RX channels. For the RX channels, there is an internal LNA, Mixer and filter before the 12-bit ADC and a filter and FIR after, as shown in Fig. 2.5(b). Similarly, for the TX, an FIR and additional filters are situated before the 12-bit DAC which stands midway between the initial circuit and another filter, mixer and finally a power amplifier. The Adalm Pluto has an impressive amount of RF components on a single board at such low cost, small and light form factor. The device has a Xilinx Zynq FPGA for onboard processing of IQ data and interface with external processor through USB 2.0 and completely power through USB. One of minor draw backs would be the need for external data processing as the onboard FPGA is at full capacity. This would be resolved by upgrading to a high performance SDR with available FPGA cache like the USRP X30, but these devices are much larger

in size and not ideal for application in this study. For this study, the ad9364 configured for 2 independent TX and RX channels for H- and V-polarization and co- and cross-polar isolation measurements, will be used. The specifications of the RX and TX configuration and their relative performance to that of the previous system are discussed in the upcoming sections.

Aside from the new RF front-end system, a real-time data transmission and processing system is also integrated into the UAS telemetry through a custom Mavlink message. The power value is calculated by the onboard computer and RF system, which are then packaged into a custom Mavlink message and sent to the UAS. Mavlink is the open source protocol used to communicate between the UAS and the ground station and transmits sensitive messages regarding the health and status of the UAS, including and not limited to the health and status of the batteries, the position of the UAS, the current mode of the UAS, the status of the flight mission and any internal errors. The custom message is written into the UAS firmware to transmit the power received by the RF system to the ground station in addition to other existing messages, eliminating the need for additional telemetry hardware for the RF sub-system. The Mavlink message is transmitted through the 915 MHz telemetry to the ground where it is processed and decoded with the help of MavProxy and a MATLAB script, as shown in Fig. 2.4 [21]. During flight, this data is continuously received and plotted in real-time to gain a real-time understanding of the measurements and make adjustments to the experiment as needed.

2.4.1 Receiver (RX)

The receiver relies on external and internal components of the SDR, which are discussed in the previous section. Although, integrated into the same device with the transmitter to reduces the size, weight and power of the overall RF system, the RX system remains independent in operation from the TX system. The RX system uses the dual channel RX ports of the SDR, that are connected to one of the two ports on the dual polarized probe through an external LNA and filter. Once at the port, the signal is received in the SDR through the internal LNA, a mixer, a digital filter, an ADC, another filter and finally through an FIR filter inside the ADI AD9364 transceiver, as shown in Fig. 2.5 [21]. The frequency range of the RX channels is identical to the TX and ranges from 70 MHz to 6 GHz when configured as ad9364. Although, the performance of the SDR is expected to vary over the frequency, the center frequency was fixed at 3.07 GHz for this study based on application and to comply with local regulations. An internal I/Q correction and calibration is available on all channels and is enabled by default. In addition to the external 60 dB LNA, the SDR has an internal gain of over 74 dB, that can be set automatically in fast- or slow-attack mode or configured manually using the gain mode. Despite the really high internal gain maximum, distortion and noise was observed for gain values over 47 dB.

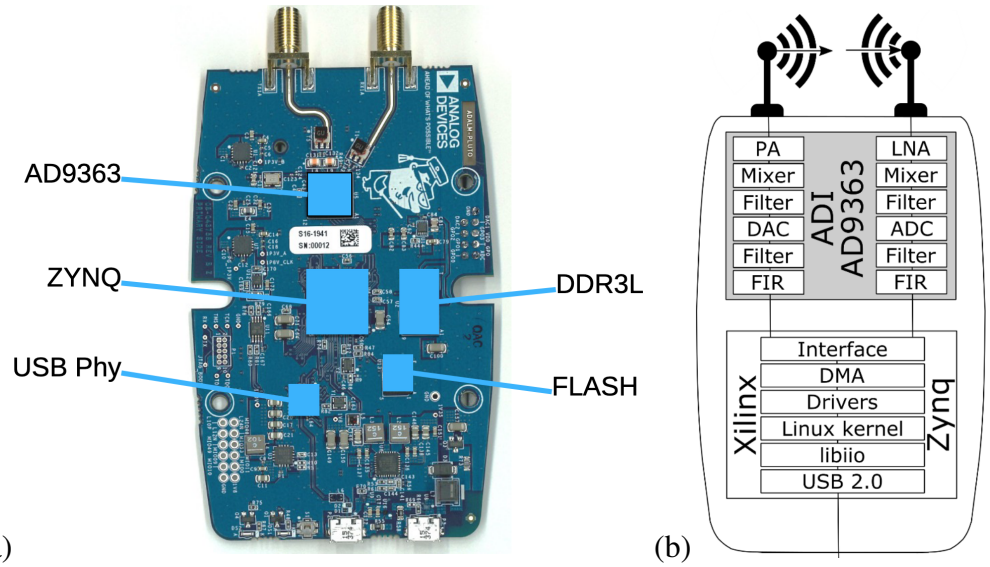

Figure 2.5: (a) Adlam Pluto SDR circuit board with labeled components shown here in the 1RX1TX configuration. The SDR is then upgraded to 2RX2TX channels with the AD9364. (b) Schematic of the SDR outlining the transceiver and Xilinx FPGA components. The design is identical between the AD9363 and AD9364 versions of the Pluto SDR.

To fix this, the internal gain was limited to 40 dB by default, assisted by the external 60 dB LNA, as mentioned earlier. The LNA is the only external component on the RX system and is integrated and powered directly from the UAS through a 5 V USB 2.0 connection. Similarly, the SDR itself interfaces with the on-board computer through a 5 V USB 2.0 connection for both power, keeping the voltage needed in the system consistent. In addition to power, the USB 2.0 connection between the SDR is the primary data connection and although, the transceiver is rated for sampling rates of over 60 MHz, the USB 2.0 connection is a bottleneck and limits the data transfer between the SDR and onboard computer. A USB 2.0 data rate is barely enough to support a maximum sampling of 7 MHz without causing loss of data and as such, the default sampling rate of the RX system is set to 5MHz to ensure data transfer integrity.

The two independent RX channels are programmed to read raw IQ data from each ports on the probe, enabling simultaneous co- and cross-polarized power measurements natively,

which is one of the major design requirements set in Chapter I. However, simultaneous RF measurements present several challenges, including channel isolation and calibration. These challenges are addressed in the next section.

In addition to co- and cross-polar measurements, the RX system is also able to switch between H- and V-polarization. This requires an additional electromagnetic RF switch circuit with over 80 dB cross-polarization isolation and a 25V electrical circuit, which enable real-time in flight polarization switching. The details of this circuit are discussed in the following sections.

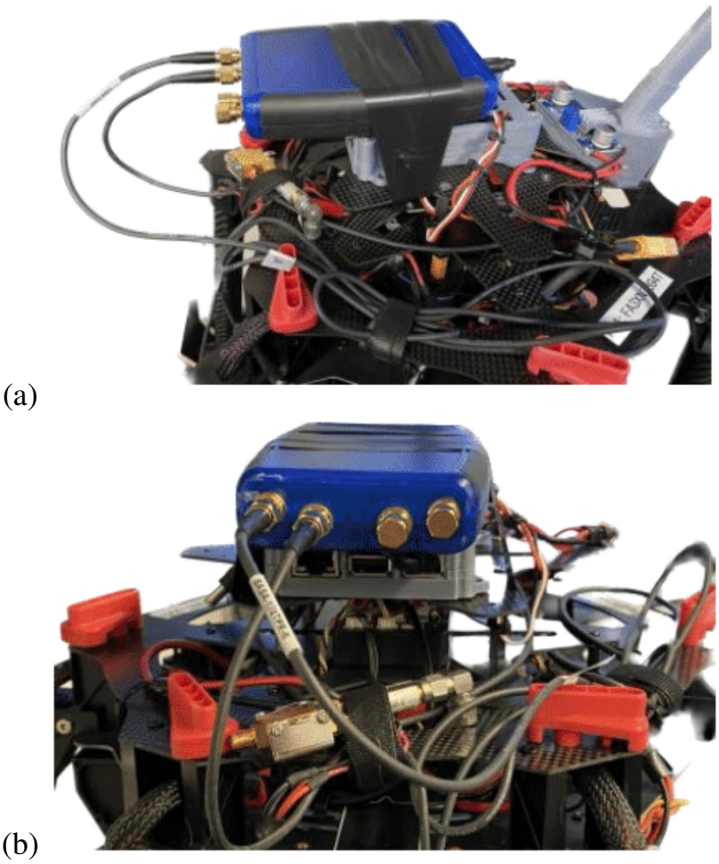

(a)

(b)

Figure 2.6: Adlam Pluto based font-end sub-system prototype here configured in simultaneous co- and cross-polar RX mode through two independent RX channels connected to the H- and V-polarization ports of the probe.

2.4.1.1 RF System Channel Isolation

When measuring co- and cross-polar power isolation simultaneously, with the same probe and receiver, channel isolation greater than the rated cross-polar isolation measurements is crucial to eliminate contamination between the channels. The AD9364 is rated for channel isolation of up to 55 dB [23] between the two independent RX channels, but can be operated at up to 70 dB isolation using the independent internal and external gain on each channel to reduce the power levels at each port. The channel isolation value was validated by testing the isolation between the channels with varying power inputs and refining the values in post processing through the MATLAB UI. The process of characterization of the channel isolation for the two RX ports is as follows. First, the RX channel 2 was terminated using a 50 Ω load while RX channel 1 was connected to a variable power source. The outputs from both channels was monitored as a known power was input from the variable power source into RX channel 1, as shown in Fig. 2.7. The power input on channel 1 was then increased in fixed increment, in this case by 5 dBm. The process was repeated until an obvious coupling between the channels was observed. From Fig. 2.7, the initial power input was -37 dBm, which is the minimum output of the variable power output source. Channel 2 remains isolated from channel 1 at the noise floor of -80 dBm and there is no observable coupling between the channels. This establishes a channel isolation of at least 30 dB. As the input power on channel 1 increases to -20 dBm, a very obvious coupling between the channels can be observed as the power on channel 2 increases to an average of -74 dBm, giving a channel isolation of 54 dB. The trend continues for succeeding increments of power input and the isolation remains fixed at an average of 54 dB, which is inline with the isolation presented in the ad9364 datasheet.

By adjusting the gain on each channel, the isolation can be further boosted at the expense of co-polar SNR to up to 70 dB. This is achieved by either attenuating or decreasing the co-polar channel external LNA gain by up to 30 dB while keeping the cross-polar port gain 30 dB higher at the initial 60 dB. The system is as such rated to measure -75 dB cross-polar isolation in this configuration before being saturated by the co-polar power. As expected, the power at the port for the co-polar is 30 dB lower and can be adjusted in the MATLAB UI or in post processing to account for the 30 dB attenuation and get a more accurate result. This technique however, permanently reduce the SNR on the co-polar port by 30 dB while the SNR for the cross-polar measurement remains unchanged. For the measurements in this paper all data collected in this configuration would be limited to -60 dB in plots, which is 20 dB lower than the expected AUT performance of -42 dB cross-polar isolation.

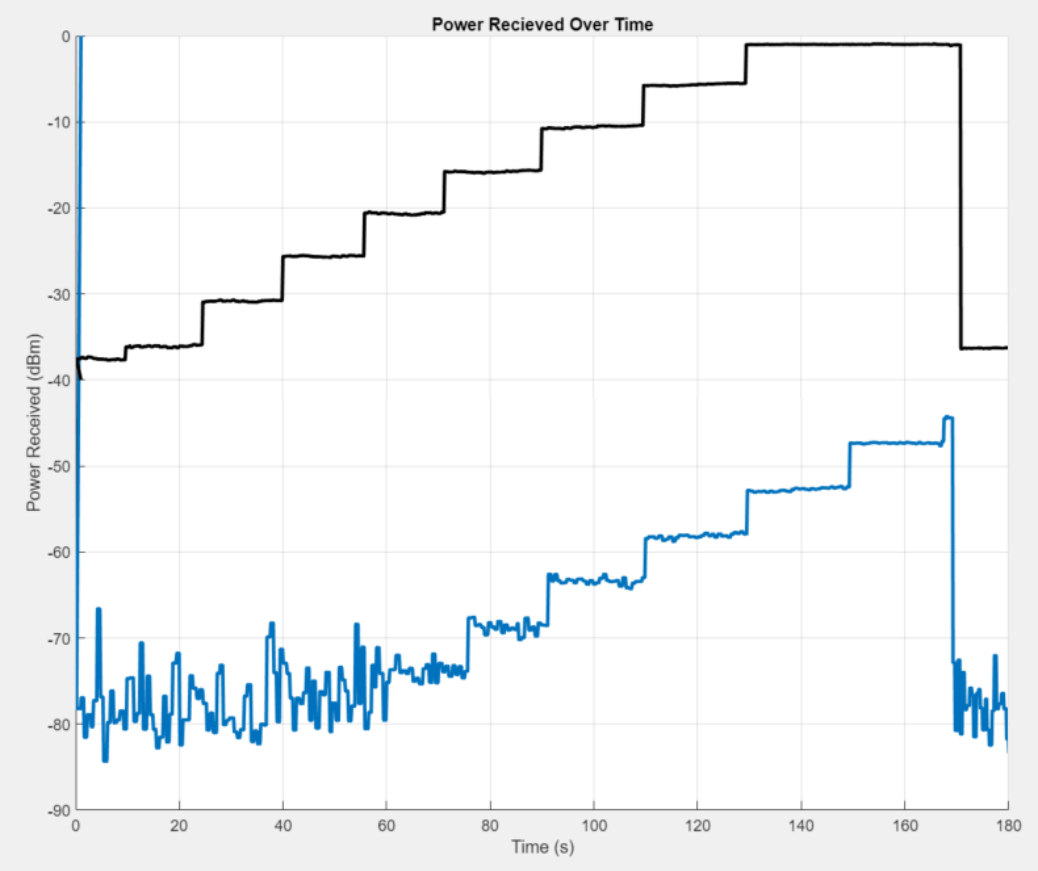

Figure 2.7: Channel isolation of the two independent RX channel on the SDR measuring co- and cross-polar simultaneously. The channels are interchangeable between co- and cross-polar isolation, in this case, the black plot is the co-polar and the blue plot is the cross-polarl measurement. The presented data is the stock SDR channel isolation, measuring at 53 dB compared to the 55 dB datasheet value.

2.4.2 Transmitter (TX)

In previous implementations, a TX system completely independent of the RX system was used which was based around a signal generator, like a Windfreak Technologies SynthHD, a dual channel tunable RF signal generator. The generator could be programmed to transmit CW or pulse at a specific frequency with different phases using the dual independent channels to create a quadrature signal output. The SynthHD has a non-volatile on-board flash memory that could be programmed for field measurement before flight. However, there was no way of modifying said system during flight or switch polarization of the TX radiation. The matter of polarization was handled by the use of the 'Twitching Eye of Horus, or Twitchy', a custom circuit consisting of capacitors, a 555 timer, and an RF switch that controlled the input signal to generate H- and V-polarized signals alternately in the order of a fraction of a millisecond, with an isolation of 40 dB [19]. For the current system, there is a transmitter build into the SDR that can be used as a source instead of relying on a signal generator. The issue of control over the H- and V-polarization can be resolved by using the two independent TX channels. Twitchy was a great implementation as it enabled transmission in both orthogonal polarization during the same mission, thus allowing at the minimum a twofold improvement in measurement time and with collocated transmitter locations but at the expense of the additional signal post-processing. This could have been further improved if there was a way to switch between polarization in real time during flight which would give us a better control over the polarization and eliminate the need for post processing.

In the new proposed system, the TX is handled in the same system as the RX using two of the four independent channels. Addressing the drawbacks first, the SDR has an overall lower output power of just under 8 dBm at 3 GHz compared to a dedicated signal generator that can output over 20 dBm natively. This is overcome by the addition of an

external amplifier, which boosts the output power by over 30 dBm to a total output power of 38 dBm. Unlike the Windfreak, the SDR is not limited to CW and simple pulse waveform and provides a lot more control over the transmitted pulse and CW signals as any waveform within the specification of the SDR transceiver can be generated and transmitted by the on-board computer, such as an LFM or Barker. In addition, there is a real time control over the two TX output channels and they can be programmed to transmit in single or dual polarization. As such, the flight could start with TX in V-polarization and once completed, could very easily be switched to H-polarization mid flight, eliminating the need for physical alteration to the system and the need for any post processing, thus streamlining the results. The new TX system can also perform almost all functions of the previous system and with a higher gain, lower overall weight and much lower power draw as it can be very simply be reverted by adding Twitchy to one of the TX channels.

Most modern spectrum analyzers allow measurement of power within a frequency range called the channel bandwidth. Such analyzers make many small power measurements across a frequency range. Although this would vary between SDRs, the channel bandwidth for the Pluto is as shown in Fig. 2.8 [21].

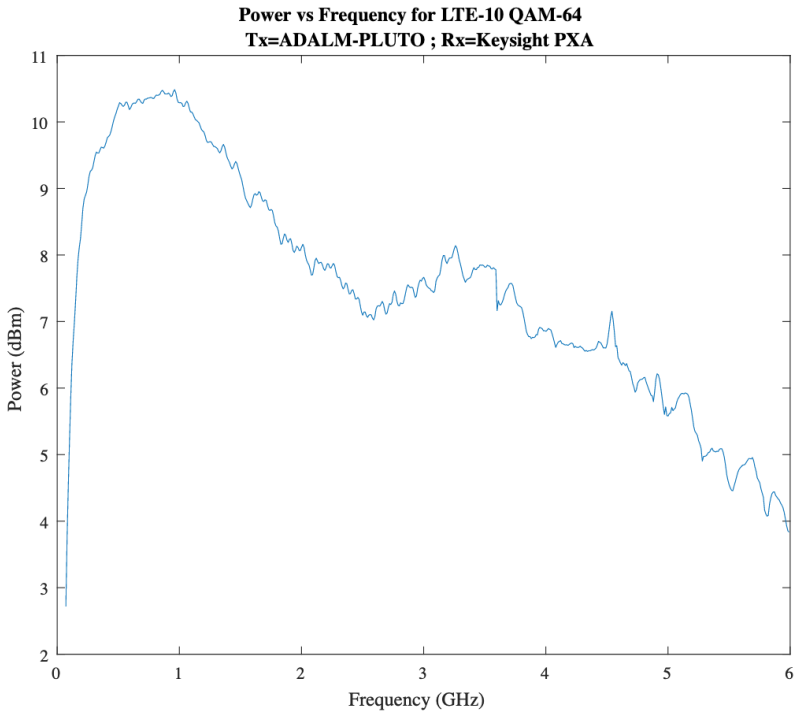

Figure 2.8: The channel bandwidth of ad9364. It shows the variation of the maximum TX power output with frequency with power output at 3 GHz of about 8 dBm.

2.4.3 Electro-Mechanical RF Polarization Switch System

The system has two possible switch configurations based on the nature of measurements being conducted. If simultaneous transmission and reception in both the vertical and horizontal polarization is needed, a two switch system is implemented which is the default configuration and shown in Fig. 2.9. In this configuration, two low noise RF switches, numbered A and B for illustration purposes, are used. Switch A is connected to the V-polarization port of the probe while switch B is connected to the H-polarization port. Depending on how the switches are powered and by controlling the RX and TX state from the SDR electronically, the system can be configured into one of four modes, as shown in Fig. 2.9. When both switches are powered off, the switches enter state 00 which is the default state to minimize power consumption. In this state, the V-polarization

port connects to RX_0 while port H-polarization port connects to RX_1, which are the first and second receive channels, respectively. Meanwhile, both transmission channels TX_0, TX_1 are terminated with a 50 Ω load. This enables the SDR to read the IQ data from both ports simultaneously and independently which is how the simultaneous co- and cross-polar power measurements can be done. In addition, since all the raw IQ data is stores in a matrix on the UAS and ground station, the co- and cross-polar power data is already accurately overlapped and does not need post processing or overlapping to visualize. For the next state, switch B must be turned on for the system to enter state 01. As seen in Fig. 2.9, the V-polarization port remains connected to RX_0 while the H-polarization port connects to TX_1, the second transmission channel. The RX_1 is connected to the terminated port of switch B. Although, technically this configuration transmits in the H-polarization while receiving in the V-polarization, since the RF sub-system has a complete control over the RX and TX channels through the SDR and either channel can be disabled to get TX in the H-polarization or RX in the V-polarization. Such a configuration is already pre-programmed into the onboard computer and triggered using a dedicated control on the UAS radio controller. The next state, 10 is very similar to state 01, where switch A, by extension the V-polarization port, is powered and connected to TX_0 while Switch B is turned off and the H-polarization port connects to RX_1. Similar restrictions to that of state 01 apply and one of channels must be disabled from the SDR to avoid contamination between the channels. State 01 and 10 are primarily designed to switch the TX in H- or V-polarization and are not ideal for RX application. All reception is conducted in state 00, which is completely isolated from both TX channels as when powered off, the RF switches connect TX channels to the terminated ports. The final state is 11, where both switches A and B are powered and connect both the V- and H-polarization ports to TX_0 and TX_1, respectively. This state enables simultaneous transmission in both polarization which has very few applications except certain phase measurement techniques, which are not the relevant to this study but

under study in other applications. In this configuration, the RX ports are automatically terminated, enabling TX radiation in either polarization. The only drawback of this configuration is the added bulk and weight of the two electro-mechanical RF switches, which increases the takeoff weight of the UAS and reduces maneuverability and flight time.

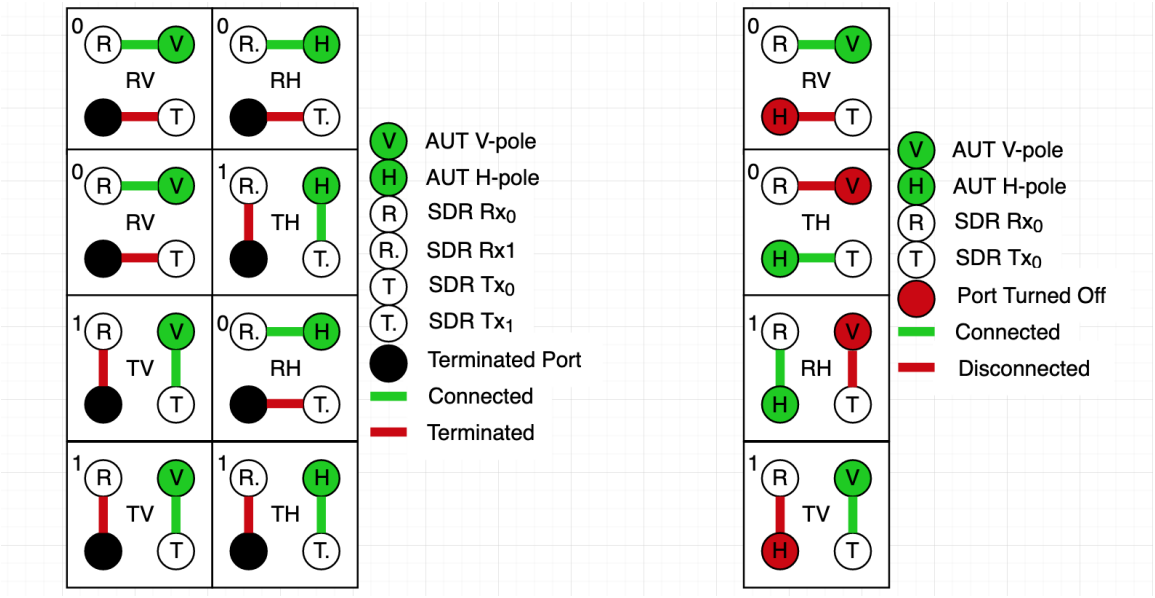

Figure 2.9: Map of switch function while switching between RX and TX in H- and V-polarization. The left shows a double switch implementation which enable simultaneous co- and cross-polar measurements, where the first bit controls the V-polarization and the second the H-polarization. Depending on the bit value, the port can be set to TX or RX while terminating the unused port, with the default mode 00 being the simultaneous co- and cross-polar RX. A single switch implementation without port termination is shown on the right.

Since the most important states of the system are state 00 for simultaneous reception and 01 and 10 for transmission in and V- and H-polarization, the system can be further simplified by reducing the number of switches at the expense of the simultaneous reception of co- and cross-polar measurements. Reducing the number of switches also reduces the overall sophistication of the system and system noise. It also decreased the takeoff payload of the UAS, yielding a longer flight time and better maneuverability. Many of the short comes of such a configuration can be overcome by simple flight mission plan changes.

For instance, given the expected repeatability of the measurement, the cross-polar can be measured in a separate mission and then overlapped with the co-polar in post processing. This configuration only uses one switch and still functions in switching the RX and TX channels between H- and V-polarization, however, only one channels is operational at a time. This means, taking co- and cross-polar measurements one at a time. Although this greatly reduces the sophistication of the system, post processing of the data is needed to overlap the co- and cross-polar patterns.

The system was implemented on test bed successfully in both configurations. As discussed earlier, the switch is a low-loss RF switch with a rated isolation of over 90 dB in S-band, which makes it ideal for dual channel RF measurements. The switch operates at 25 V, which is much higher than the operating voltage of the rest of the circuit, 5 V. It is however within the maximum voltage available on the UAS, which is the operational voltage of the UAS. Since the UAS is a delicate system, great care needs to be taken when implementing devices that operate at higher voltage or currents. This is why, even though the switch system was completely functional on the test bed, its implementation remained limited on the UAS as more testing was required. Fig. 2.10 [21] shows the final switch circuit and implementation on the test bed and Fig. 2.2(b) shows the switch system as integrated into the UAS.

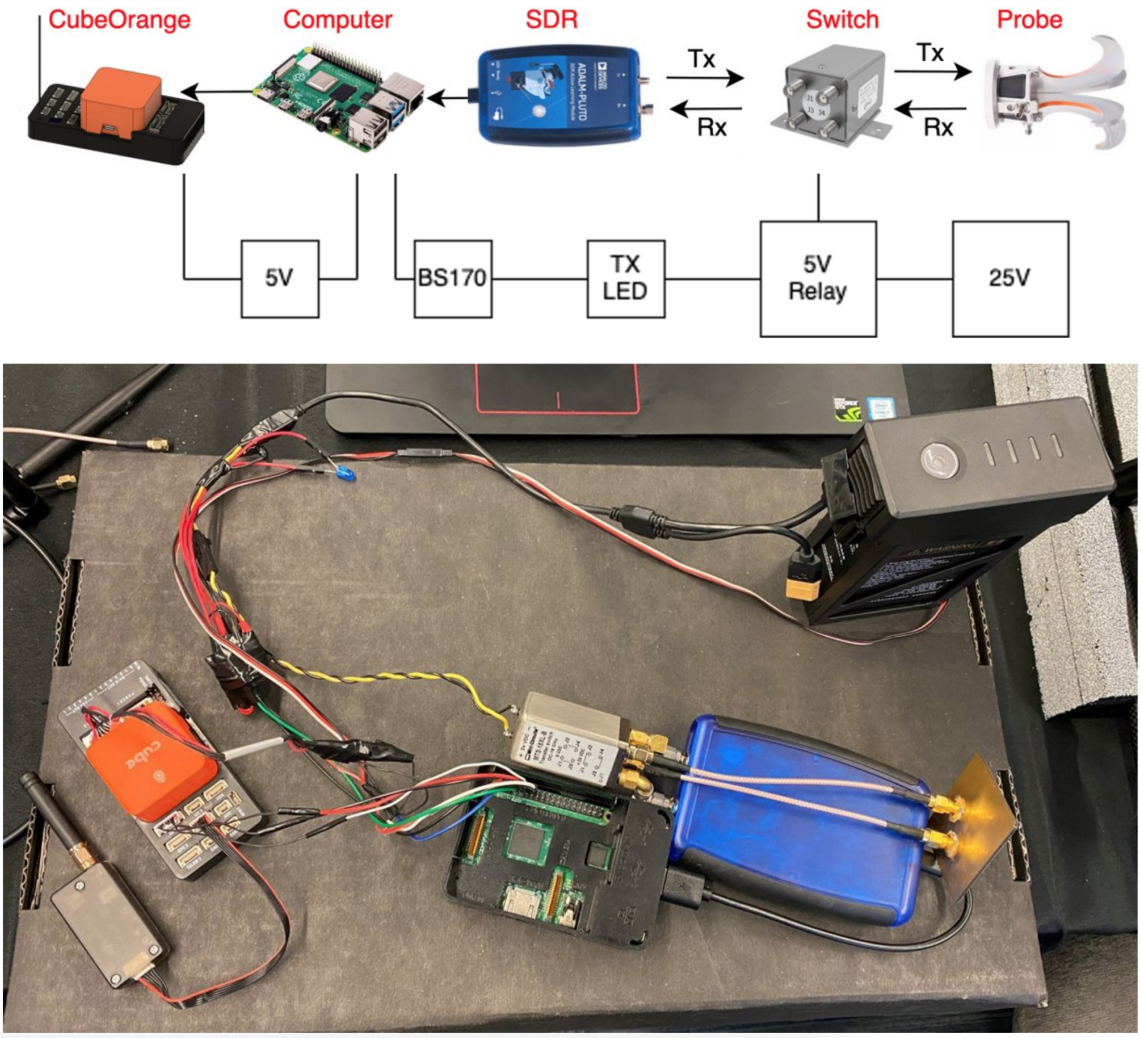

Figure 2.10: The final circuit and implementation of the switch system. The top image illustrates the circuit controlling and powering the switch through a MOSFET. The switch is operated from the radio controller on the ground which communicates with the PixHawk. The PixHawk relays the message to the onboard computer which then control a power replay to turn the switch on or off as well as configure the SDR in RX or TX mode. The bottom images shows the implementation of the system on the test bed. The system is implemented with a single switch configuration but is also fully functional with dual switch.

2.4.4 Antenna Probe

The system was design to be versatile and modular, including compatibility with different probes. The two probes mounted and tested with the system are a wide-band open

ridged horn antenna and a custom 12 element microstrip patch antenna (Stop-Sign antenna), as shown in Fig. 2.11(a) and Fig. 2.12(a), respectively. The horn antenna is compact and more stable on the gimbal and also has a much wider frequency range of 3 GHz - 18 GHz. Looking at the radiation patterns, as provided with the datasheet, the antenna has a narrow co-polar beam but the cross-polar is just over -45 dB at broadside, as shown in Fig. 2.12(b).

(a)

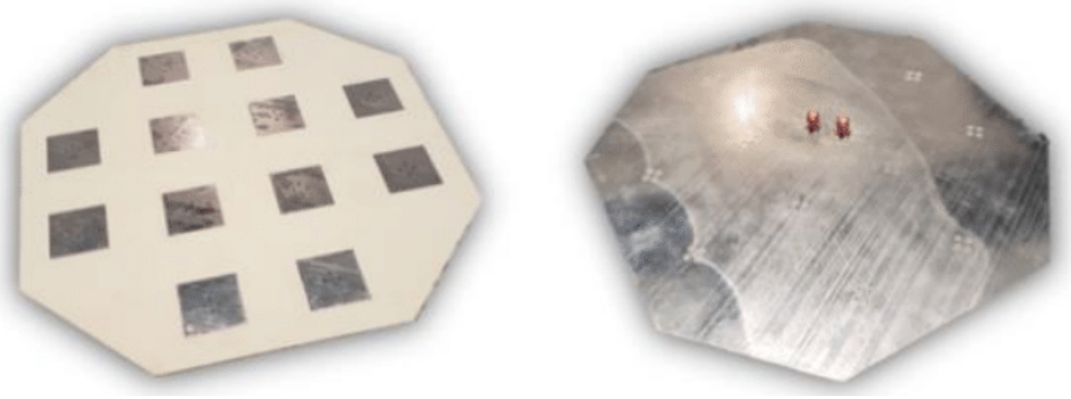

(b)

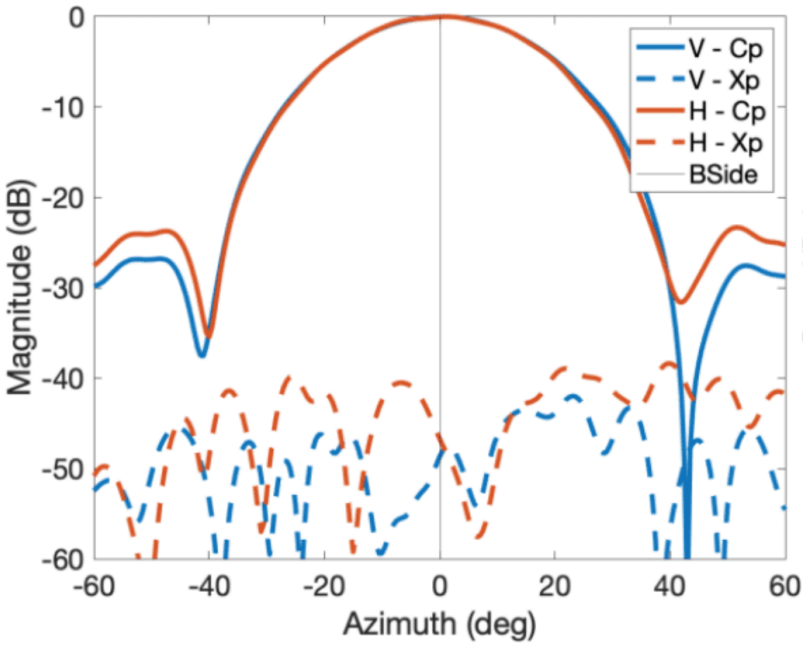

Figure 2.11: (a) Narrow-band 12-element microstrip patch planner array antenna probe. (b) The far-field radiation pattern of the 'Stop-Sign' antenna as measured in the near-field chamber. The cross-polar in is under -45 dB in the V-polarization.

Comparatively, the Stop-Sign probe is much larger in dimensions and as such not as stable on the gimbal as the horn. The bandwidth is also very narrow from 2.95 GHz-3.10 Ghz. However, the cross-polar isolation in V-polarization consistently measures just over -50 dB, as shown in Fig. 2.11(b) [21], which is much better than the horn.

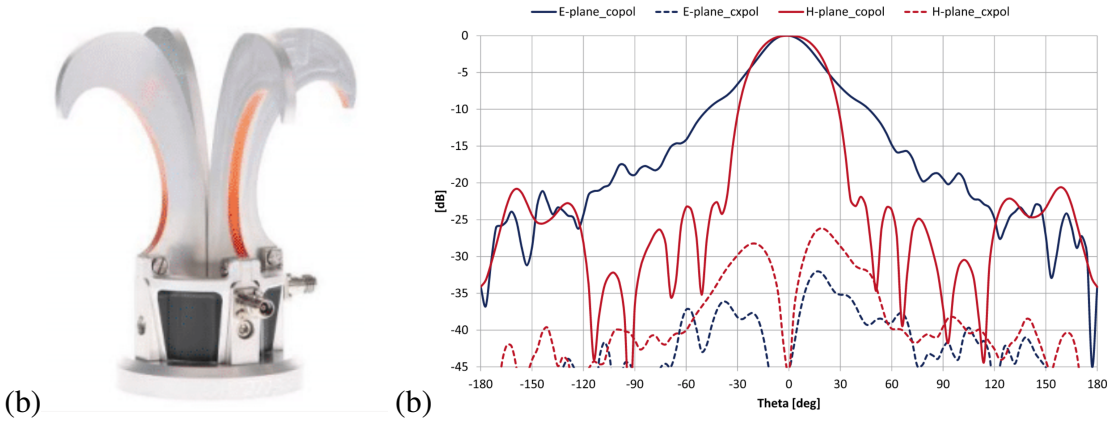

Figure 2.12: (a) Wide-band open boundary quad ridged horn antenna probe. (b) The co- and cross polar antenna patterns of the antenna as provided in the datasheet.

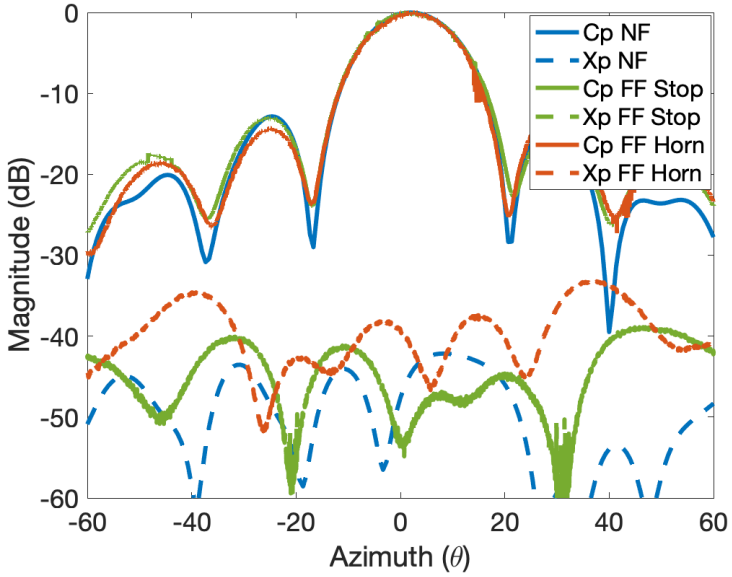

Figure 2.13: Comparing the two potential probes. First the wide-band open ridged horn antenna and the second is the 'Stop-Sign' antenna. The Co-pol performance is great with both probes but the cross-polar measurements are much better with the patch antenna. As such, the patch antenna was used for all cross-polar measurements.

A 60 ° scan of the AUT was performed at far-field in an echoic chamber with the RF sub-system using each probe and the results were compared to the far-field chamber results as control. The co-polar remained consistent between the probes as expected with nulls under -20 dB. The Stop-Sign outperformed the horn in by matching at -13 dB side lobes of the control with the horn having much lower -15 dB side lobes. The Stop-Sign also outperformed the horn in cross-polar with consistent -40 dB cross-polar while the horn had cross-polar values as high as -33 dB, as presented in Fig. 2.13.

2.5 Summary

This chapter cover the improvements and upgrades made to the UAS hardware from Chapter 1 for application in radar and antenna radiation pattern measurements. The design choices made with regards to the platform as a whole, the gimbal system and the positioning are addressed. A detailed discussion of the new SDR based RF sub-system is also provided, including details of the probe, the SDR specification, the RX system, the TX system and the RF electro-mechanical switch system that makes simultaneous co- and cross-polar measurements possible. Finally, the integration between the UAS hardware and the RF sub-system and how they work together through custom Mavlink messages is discussed. From the signal reception at the probe to the radiation pattern plot on the ground station through custom MATLAB programs is defined in detail.

Chapter 3

Setup and Measurements

In this chapter, the experimental setup to characterize the new RF front-end system and it its integration with the UAS is discussed. First, the radiation pattern of an antenna-under-test is calibrated and measured in a near-field anechoic chamber, serving as a baseline reference for all subsequent measurements. Subsequently, the AUT is evaluated in a far-field chamber, both with and without the presence of the UAS, to investigate the influence of the UAS on the co- and cross-polar radiation patterns measurements of the calibrated AUT. Additionally, an outdoor setup similar to the experimental setup of the far-field chamber is replicated to examine the impact of non-ideal conditions, ground reflection, and multi-path on the co- and cross-polar radiation patterns of the AUT with the standalone RF front-end system and the system as integrated into the UAS. Lastly, a flight test of the UAS equipped with the new RF system and the real-time measurement suit is conducted, facilitating the characterization of the AUT once again in both co- and cross-polar to complete the characterization of the front-end system.

3.1 Frequency of Operation

The Adalm Pluto SDR and the integrated transceiver ad9364 are rated for operation in the frequency range of 325 MHz to 3.8 Ghz at 61 Mhz sampling rate in the ad9363 firmware configuration. The only components limiting operation in this range are the LNA and power amplifiers, which are rated for S-band only. When connected with the RF sub-system without the external amplifier circuit, the SDR operates fully in the rated frequency range. The only exception being the affects of the such configuration on the SNR of the received signal, which is discussed in the next section. The frequency range of the SDR can be extended at the expense of sampling rate to operate from 75 MHz to 6 GHz, however, at the expense of lowering the sampling rate from over 61 MHz to just under 32 MHz. This is done by updating the SDR from the ad9363 compatible firmware to the ad9364 firmware that unlocks the complete specification of the ad9364. The system is now rated for 75 MHz to 6 GHz without the external amplifier circuit with a slight frequency dependent variation in performance. This can observed with the TX output as shown in Fig. **??**, illustrating the dependency of transmit power on frequency.

Given the system is primarily designed for S-Band weather radar systems, the center frequency for the new RF front-end system system is set at 3.07 Ghz both for compatibility with the S-band radar and to conform with local and FAA spectrum rules. Based on the center frequency, the external amplifier circuit has a bandwidth of 1 Ghz. This puts the effective frequency range of the system with the external amplifier circuit at about 2.5 GHz to 3.5 GHz.

3.2 Antenna Under Test (AUT)

The system is designed for wide-band application but was primarily tested at 3.07 GHz to focus on S-Band phased array weather radars. As such, the AUTs are similar in design and performance to these radar systems. Since phased array antenna are sophisticated systems and must be calibrated for optimal performance, all AUTs were calibrated in an anechoic chamber before field measurements. Of the several S-Band AUTs tested during the development of this system, results from only two AUTs, 8x1 probe fed array and 8x1 aperture coupled array, will be discussed. Both antenna arrays are based on an S-band dual polarized microstrip patch antenna as shown in Fig. 3.1. The arrays are controlled and calibrated by a custom MATLAB application that provides high resolution control over phase and amplitude of individual elements in the array. The arrays can be programmed to scan or transmit at a fixed angle in real-time. Although, these are fully functional phased array antenna, all measurements for this study are done at broadside with uniform distribution to stay consistent between measurements.

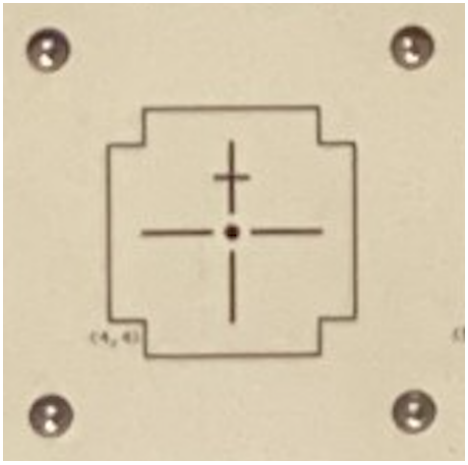

Figure 3.1: S-band dual polarized microstrip patch antenna unit cell which is base for all AUTs

3.2.1 Probe Fed Phased Array

The microstrip patch phased array array has a relatively simple design with a single transducer with 16 outputs, 8 of which are reserved for H-polarization ports and the other 8 for V-polarization ports of the array. Although the unit has a total of 16 probe fed elements, as shown in Fig. 3.2(a), only 8-elements in the top row are excited in dual polarized configuration using the 16 transducer ports. The array is completely wireless, compact, lightweight and mobile, which makes it very convenient to measure and characterize in an anechoic chamber and is ideal for field testing. The radiation pattern are well defined in co-polar but the cross-polar performance is held back by the dual probe feeds, which only have an isolation of 33 dB, non-ideal for cross-polar measurements on under 40 dB as the cross-polar for the array is just under 30 dB. Hence, this array is primarily used for co-polar radiation patterns validation. The calibrated co- and cross-polar patterns are as shown in Fig. 3.3(b).

Figure 3.2: Probe fed dual pole 8x1 phased array unit under test in an anechoic chamber.

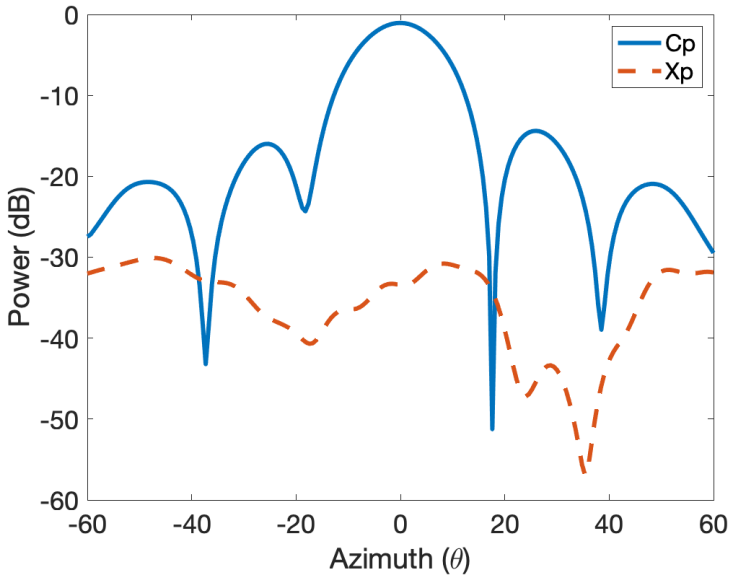

Figure 3.3: The near field to far-field radiation pattern for the AUT.

3.2.2 Aperture Coupled Phased Array

As discussed earlier, phased array antenna with -40 dB cross-polar isolation are challenging to design, fabricate and calibrate. Although, the previous AUT was within the specification for co-polar measurements, for the cross-polar isolation measurements a more reliable AUT is needed. This array is upgrades from the probe feed inputs to an aperture coupled feeding mechanism, which greatly improves the cross-polar isolation performance. The back end transducer setup is similar to the previous array and of the 64-elements shown in Fig. 3.4(a), only 8-elements in the middle row are excited using the 16 ports from the transducers. Although, the phased array is completely wireless and provides high resolution control over phase and amplitude of individual elements for calibration, it is relatively large, heavy and bulky. The calibrated co- and cross-polar radiation patterns, as shown in Fig. 3.5, highlighting the consistent cross-pole isolation of under -40 dB, which meet the requirement for this study.

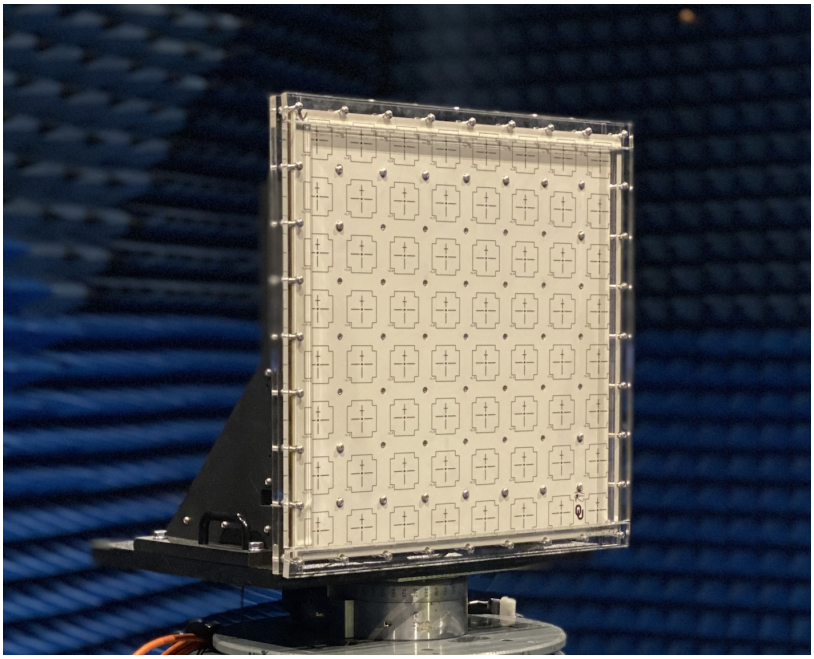

Figure 3.4: Aperture coupled 8x1 dual polarization phased array unit under test in an anechoic chamber.

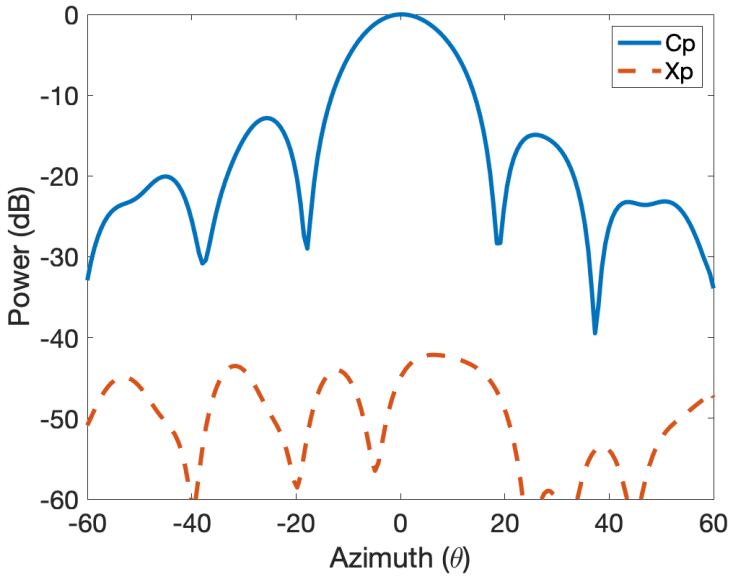

Figure 3.5: The near field to far-field radiation pattern for the 8x1 aperture coupled AUT.

3.3 Modes of Operation

With the current implementation, UAS primarily measures a single cut of the radiation pattern of the AUT in either the E- or the H-plane. For this study, the AUT was excited in the V-polarization and only a single cut in the E-plane was measured. As such, the UAS also measure just a single E-plane cut of the pattern, although in multiple measurements. The following tests were conducted to fully characterize the performance of the new front-end system and its integration with the overall UAS design.

- Calibration and Characterization of the AUT in the Near-Field Chamber:

  The AUT was calibrated using a custom MATLAB program with high resolution control over the amplitude and phase of individual elements through the back end transducer. Once calibrated, near-field to far-field conversion was used to obtain the calibrated far-field radiation patterns of the AUT to be used as a baseline measurement.

- Far-Field Chamber AUT Characterization:

  The AUT was characterized in a far-field chamber with the new front-end system as a standalone system and then as an integrated part of the UAS to measure any variation in performance.

- Outdoor AUT Characterization:

  The AUT was also characterized outdoors in similar experimental setup as the far-field chamber, with and without the UAS to measure the realistic performance of the system with several environmental factors included.

- In-flight AUT Characterization:

  Lastly, an in-flight test was done to test all systems of the UAS and get real-time as

well as higher resolution data from the UAS. The experimental setup was slightly different but the primary focus of this test was to ensure proper function of all components of the UAS and the RF font-end system.

3.3.1 Near-Field Chamber AUT characterization

This measurement is the true radiation patterns of the AUT and is measured externally with the sophisticated components of the a near-field chamber. In the chamber, the AUT is isolated from almost all external factors like ground reflections and multi path. Furthermore, it is also not affected by any design flaws or systematic errors due to integration with the UAS. The test yielded calibrated radiation patterns of the AUT that are used as a baseline for all measurements done with the RF system.

The AUT was placed 12 inces from the near-field S-band probe rated for 2.8 GHz to 3.2 GHz. All SMA connection were covered with a metallic copper take and with non-reflective foam to reduce reflections and contamination. The AUT was aligned with the probe using lasers and verified with different built-in techniques within the chamber.

The array was calibrated in amplitude and phase, element by element, using a custom MATLAB program. The scanning range for the chamber was set at 60 deg in azimuth and 60 deg in elevation from the center of the array.

3.3.2 Far-Field Chamber AUT characterization

Similar to the NF chamber, this FF chamber is also isolated from all reflections and provides the more accurate radiation pattern of the AUT. Unlike the NF chamber, none of the FF chamber equipment was used and all measurements were done with the new RF system and eventually with the RF system as integrated with the UAS.

The chamber has two non-reflective poles that are 25 ft apart as shown in Fig. 3.6, which support the AUT on one end and the probe with the RF font-end system and UAS on the other end. All measure of the AUT here onwards are in true far-field. The poles supporting the probe and AUT are 90 in from the ground and can be lifted further 50 in to the specular region. All measurement were done in the specular region to get the best results. The probe was put on a fixed pole, while the AUT rotates horizontally as shown in Fig. 3.6. The AUT and the probe were aligned to be at broadside and 0 deg elevation with lasers mounts on the chamber walls and the 5 nW laser mounted on the UAS. The measured cut is the E-plane of the V-polarized AUT. Once the measurement was complete, the probe was mounted on the UAS and the measurement was repeated.

The primary focus of this setup is to measure any performance differences between the RF front-end system as a standalone system versus when integrated on to a UAS. This would be essential is investigating the affects of the UAS hardware on the performance of the RF front-end system.

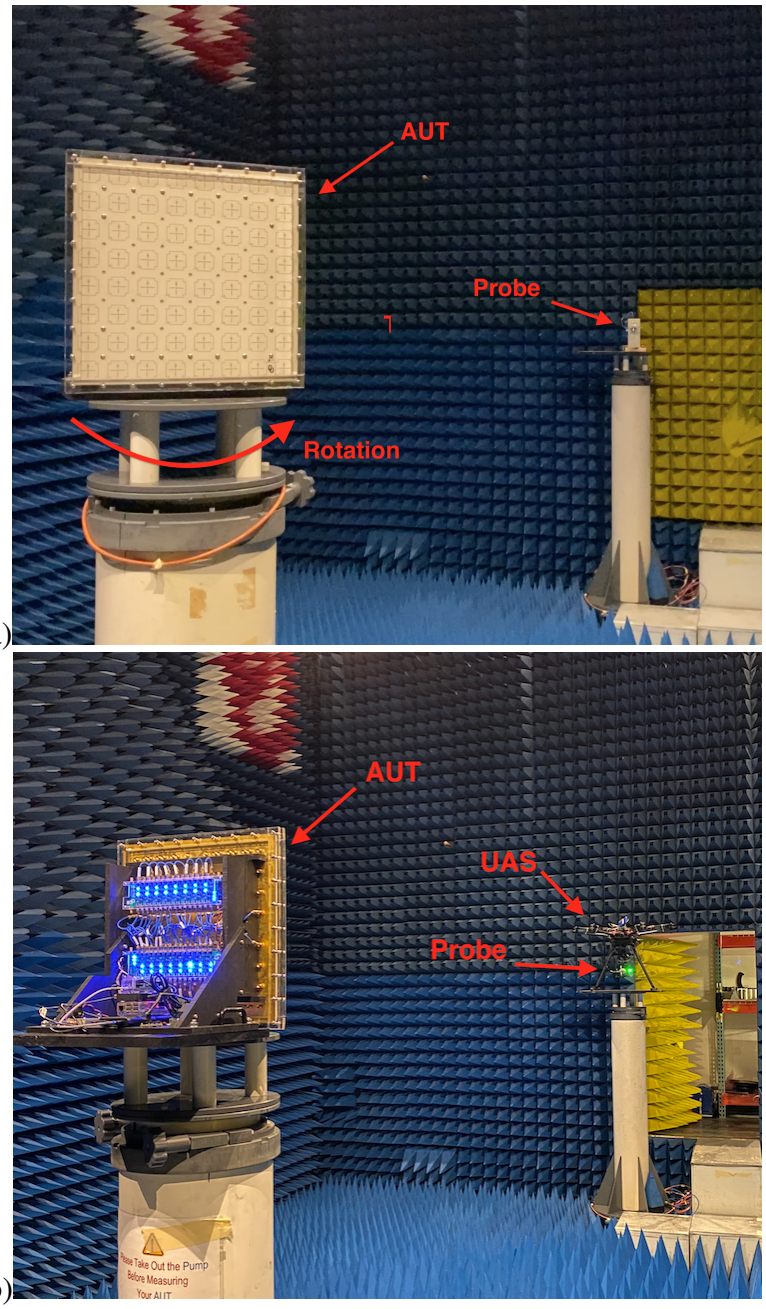

Figure 3.6: The RF sub-system test setup inside a far-field anechoic chamber. The AUT is an aperture coupled 1x8 microstrip patch phased array antenna at broadside with cross-polar isolation performance of under -40 dB. (a) The RF sub-system as a standalone without the UAS, as mounted on a non-reflective mount. (b) The RF sub-system in final configuration as mounted on a UAS. To note, the figures show the setup in the non-specular region, but measurements were conducted at 150 in, in the specular region after alignment with lasers. The landing gear for the UAV was deployed for all chamber measurements but was measured both in retracted and deployed more for outdoor measurements.

3.3.3 Outdoor AUT Characterization

This test replicates the far-field chamber measurements in similar experimental setup but in non-ideal environment. The measurement was conducted in an open field, however, there were a few metallic structure and a building in the surrounding which are commonly present in the operational environments of weather radars. The poles supporting the AUT and UAS were metallic as non-reflection poles strong enough to support at the AUT and rotary table were not available. Similar to the far-field chamber, the poles were 25 ft apart and raised 90+50 in to keep the experimental setup consistent. The AUT was mounted onto a metallic rotary table and controlled from a custom software to replicate the scanning speed of the chamber scanner. A custom mount was built to mount the AUT to the rotary table to replicate the scanning capabilities of the far-field chamber outside. The alignment process was also exactly the same as the far-field chamber and done meticulously with a laser until the probe and AUT were aligned at 0 deg elevation and broadside. The rotary table was controlled with a Velmex controller while the probe remained fixed. Once the measurement was complete, the probe was mounted on the UAS and the UAS was programmed to hover at the exact location of the probe.

Similar to the far-field chamber measurements, the focus of this setup is also to measure any performance differences between the RF front-end system as a standalone system versus when integrated on to a UAS in the real operational environment. This would be essential is investigating the affects of the UAS hardware on the performance of the RF front-end system.

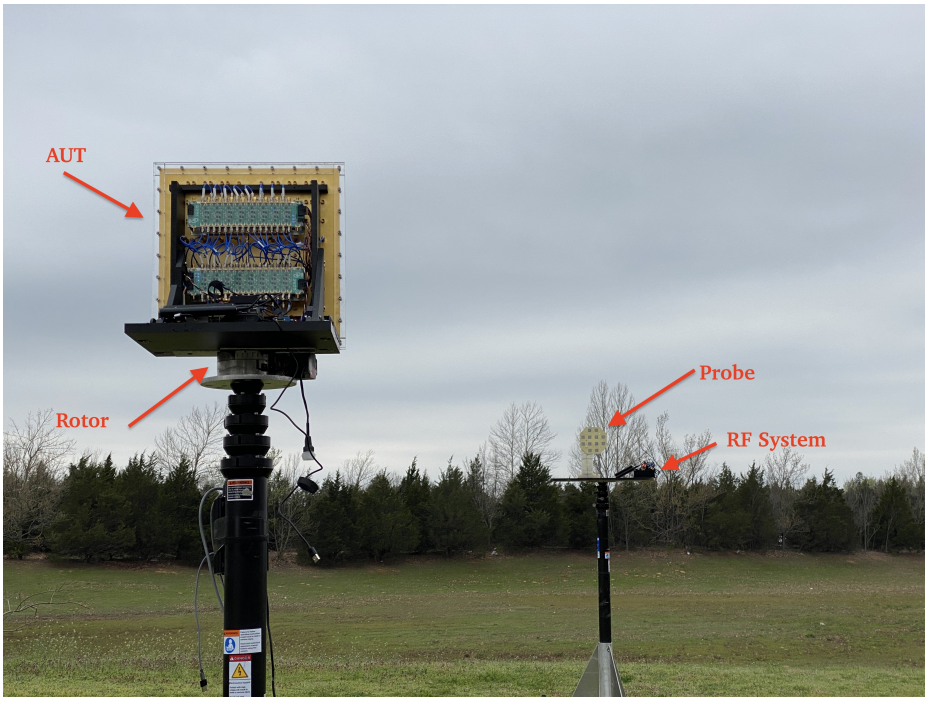

Figure 3.7: The chamber measurements being replicated outdoors. The AUT and Probe are aligned with a laser, raised at 150 in. The AUT remains the aperture coupled 1x8 microstrip patch phased array antenna at broadside but the probe in the figure is a custom S-band microstrip patch antenna array. The measurement were repeated with the standalone RF sub-system and the UAS.

3.3.4 In-Flight AUT Characterization

As the performance of the RF front-end system and UAS are investigated in the previous two setups, an in-flight test was needed to test the UAS system as a whole, with the gimbal, real-time data measurements and switching capabilities. Since the characterization with the standalone RF system was not an option, this test was only done with the UAS and as such the experimental setup is slightly different. The test was designed to be as close to the operations conditions of the system as possible with all but the switch system engaged. (As discussed earlier, the operational voltage of the RF switch was very close to the operational voltage of the UAS. To ensure flight safety, flights with the switch system engaged were limited.) The AUT was positioned to radiation vertically to reduce ground reflection

and multi-path as the UAS measured a cut directly above the AUT, this setup is much closer to the chamber setup and the outdoor measurement but such measurements are ideal and possible with actual S-band weather radar, alongside a 45 scanning. The AUT was radiating in V-polarization at broadside and the UAS measured co-polar and cross-polar cuts in the E-plane. The UAS was first programmed to measure at 25 ft but due to safety concerns and higher SNR than expected, the final measurement was done at 80 m.

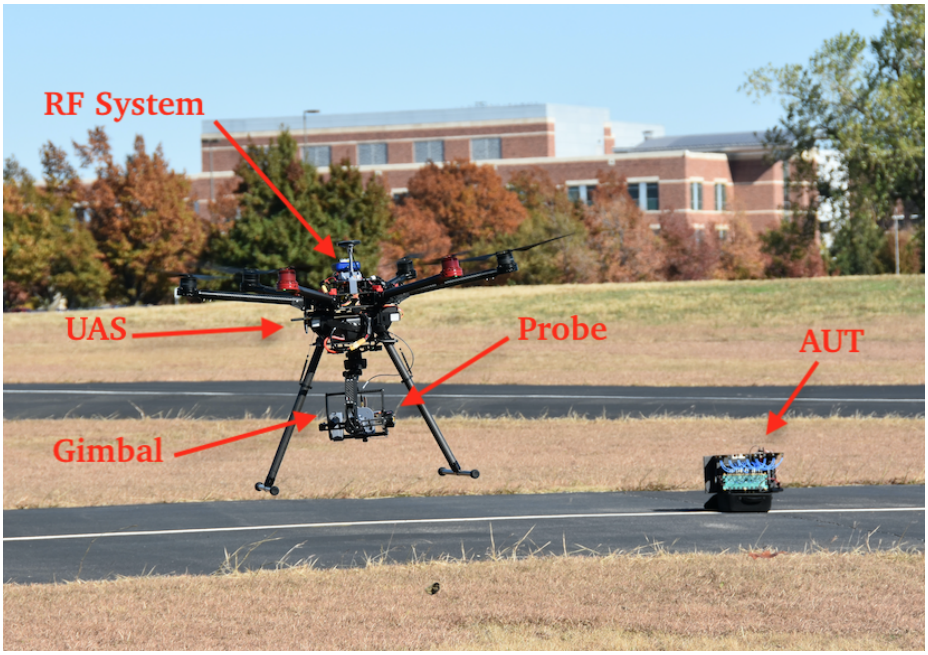

Figure 3.8: The field measurement setup with a grounded AUT in TX mode and an airborne probe in RX mode. The RF sub-system is mounted and integrated into the UAS flying cuts and grids over the vertically oriented AUT. The AUT is radiating perpendicular to the ground to reduce ground reflections and clutter. The UAS takes V-polarization, co-polar and cross-polar, measurement in a single cut in the H-plane which can be standalone measurements or done in a grid to process later.

Figure 3.9: The spherical mission plan of the UAS as visualized in 3D. This is essential in verifying the mission safety and to ensure the UAS remains at a safe distance from all structures.

3.4 Summary

This chapter focuses on the experimental setup for the antenna characterization. Firstly, the radiation frequency for the measurements is determined based on the specific requirements of the system. The chosen frequency allows for accurate characterization of the S-band AUT and aligns with the operational needs of the system as well as spectrum regulations. The chapter then discusses the selection of the antenna under test, highlighting its advantages and disadvantages. Considerations such as size, gain, and frequency range as well as cross-polarization isolation performance are taken into account to ensure compatibility with the measurement objectives. The experimental setup is described in detail, starting with the initial calibration and measurement of the phased array antenna conducted in a near-field anechoic chamber. This controlled environment provides a suitable setting for assessing the performance of the system and obtaining baseline measurements. Following the near-field measurements, the experiments are repeated in a far-field anechoic

chamber. This chamber simulates a more ideal condition by providing an unobstructed and interference-free environment for accurate measurements. To further validate the results, the measurements are also performed outdoors, replicating real-world scenarios. This step allows for the assessment of the system's performance under real environmental conditions, including the effects of natural surroundings, atmospheric conditions and the UAS hardware. Finally, a flight test is conducted to evaluate the system's performance in an operational setting. This test provides valuable insights into the system's functionality, stability, and reliability during actual airborne operation. By systematically conducting measurements in various controlled and real-world environments, the chapter establishes a comprehensive framework for evaluating the performance of the system and its ability to accurately characterize the antenna under test.

Chapter 4

Results and Validation

The results for the near-field chamber, far-field chamber, outdoor and in-flight test results are presented in this chapter. The co-polar and cross-polar isolation radiation patterns were measured at broadside in all tests to compare the variation in performance of the system in these environments. The near-field test was to calibrate the AUT and get a baselinied radiation pattern of the AUT. The far-field chamber and outdoor tests focused on the performance differences of the RF front-end sub-system due to integration with the UAS. Lastly, the in-flight test was to verify the operational readiness of the whole system.

4.1 Far-Field Chamber Measurements

Taking the measurements of the AUT from the near-field chamber as the control, the far-field chamber measured co-polar radiation patterns are very consistent with the control. The nulls are not as well defined but also remain consistent between the standalone RF subsystem and the UAS. The cross-polarization isolation value in the far-field is 8 dB higher than control but remain consistent for both the UAS and the standalone RF system. Although the nulls are not as well defined, their consistency is maintained. The presence of the UAS introduces variations in the cross-polarization patterns, however, the values remain under -40 dB, an acceptable range for this study. Overall, the far-field chamber

measurements show higher cross-polar isolation values compared to the control, which can be attributed to the performance of the probe or alignment in the far-field chamber. Despite the variations introduced by the UAS, the patterns exhibit consistency and the measurements are reliable.

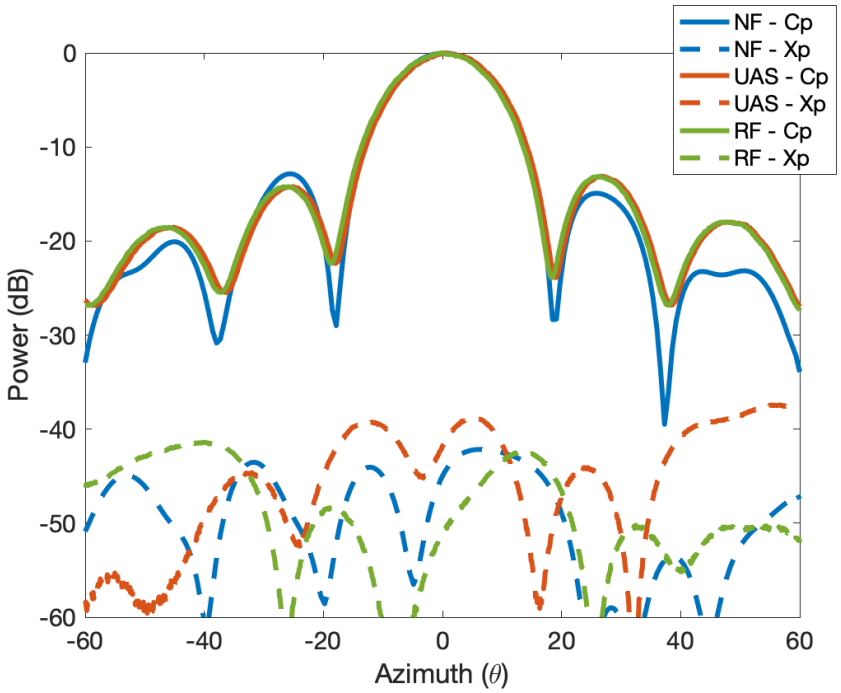

Figure 4.1: The far-field, H-plane, co- and cross-polar radiation patterns of the AUT as measured with the RF system, as RF-Cp and RF-Xp, in the anechoic chamber, compared with the near-field patterns of the AUT. The RF-System co-polar remains identical when measuring standalone or integrated into the UAS but there is a 6 dB increase in the cross-polar when integrated into the UAS, where UAS-Cp and UAS-Xp are the co- and cross-polar patterns of the integrated UAS measurements, respectively.

4.2 Outdoor Measurements

When comparing the results from the outdoor measurements to the control patterns, the co-polar pattern with the standalone RF system (RF-Cp) and UAS integrated RF system (UAS-Cp), remained consistently identical to the control, mainly due to the higher power output. However, the cross-polar isolation pattern exhibited significant differences when

the UAS was part of the system, as shown by UAS-Xp in Fig. 4.2. Ground reflection played a major role in this discrepancy. The cross-polar pattern without the UAS showed a difference of approximately 5 dB compared to the chamber value, as illustrated by RF-Xp. This increase can be attributed to external factors and ground reflections. However, with the UAS in the measurement setup, the cross-polar pattern reached as high as -33 dB, which is approximately 10 dB higher than the control value. This considerable increase in cross-polarization can be attributed not only to external and ground reflections but also to the transition from non-reflection mounts and poles to metallic mounts and poles for the outdoor setup.

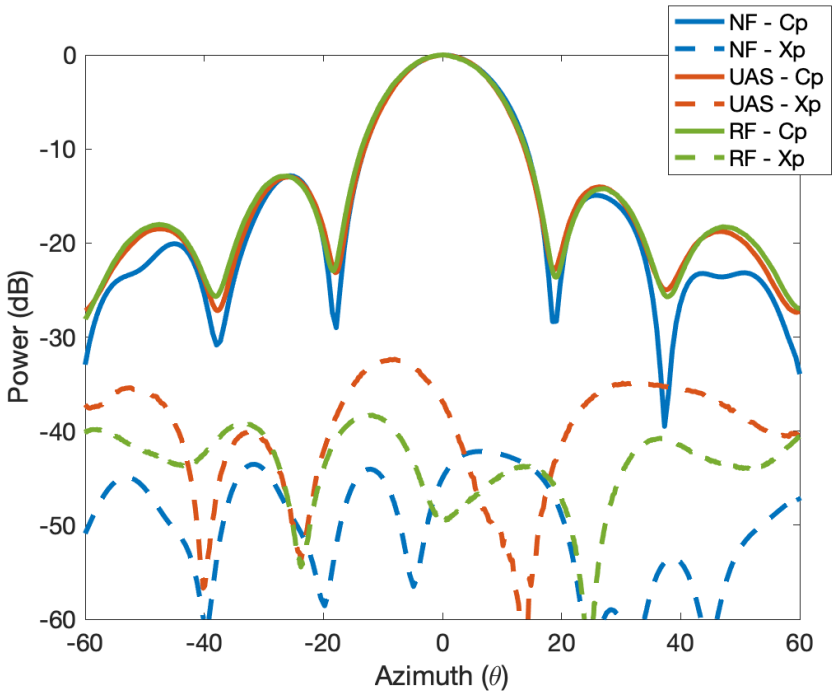

Figure 4.2: The far-field, H-plane, co-polar and cross-polar radiation patterns of the AUT as measured with the RF system in the anechoic chamber, compared with the Near-Field patterns. The RF-System Co-pol remains identical when measuring standalone or integrated into the UAS but there is a 4 dB increase in the cross-polar when integrated into the UAS.

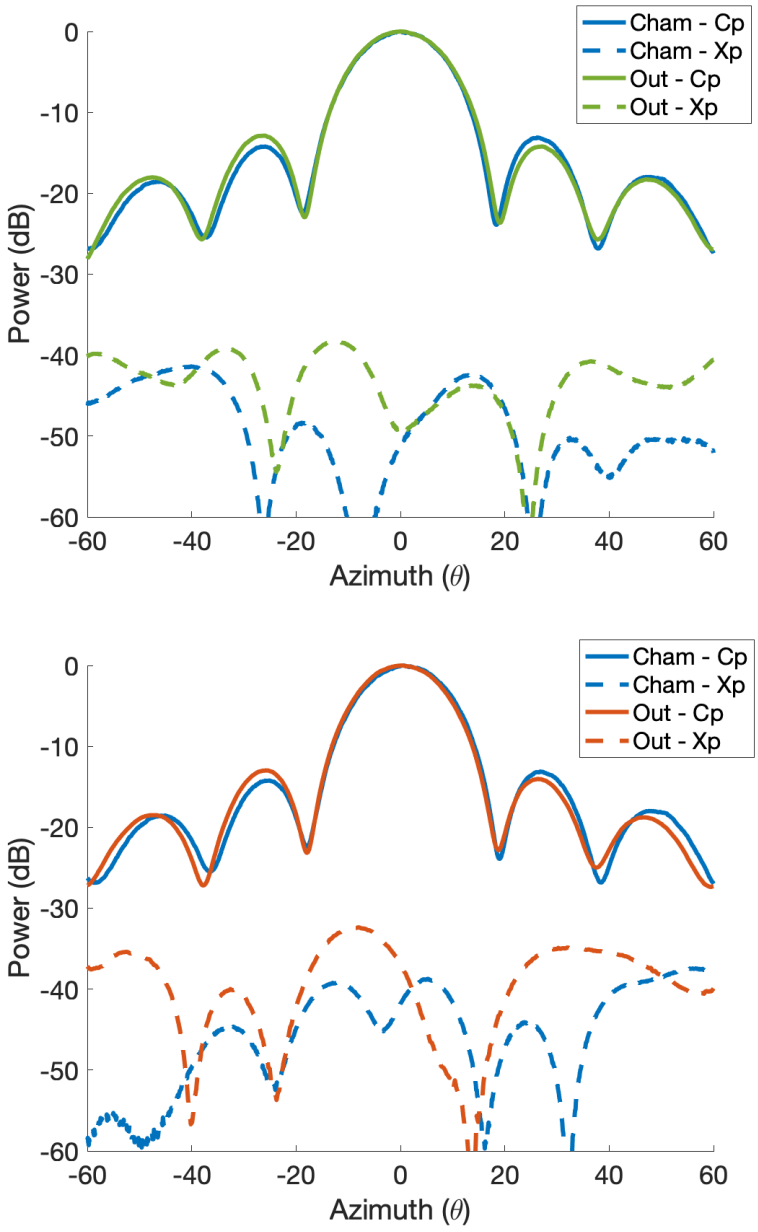

Figure 4.3: The RF sub-system test setup inside a far-field anechoic chamber. The AUT is an aperture coupled 1x8 microstrip patch phased array antenna at broadside with cross-polar performance of under -40 dB. Shown on the left, the RF sub-system as a standalone without the UAS, as mounted on a non-reflective mount. Shown on the right, the RF sub-system in final configuration as mounted on a UAS. To note, the figures show the setup in the non-specular region, but measurements were conducted at 150 in, in the specular region after alignment with lasers. The landing gear for the UAS was deployed for all chamber measurements but was measured both in retracted and deployed more for outdoor measurements.

These results were expected, considering the higher cross-polarization observed outside the chamber. The presence of the UAS further amplified the cross-polarization isolation values, highlighting its impact on the measurement. The influence of external reflections and the use of metallic poles in the outdoor setup contributed to the observed differences in cross-polarization values.

Overall, the outdoor measurements provided valuable insights into the impact of real-world conditions on the cross-polarization characteristics of the system. The discrepancy between the control values and the outdoor measurements emphasizes the importance of considering external factors, such as ground reflections, when analyzing cross-polar patterns.

After comparing the value to the control we can also compare the value of the standalone value in the chamber and outside and similarly of the UAS in the chamber and outside. As presented in Fig. 4.2 the value for the standalone increased by 3 dB but are much higher for UAS, on average an increase of 8 dB. This can be explained as the UAS its self is a major reflector when outside hovering near metallic structure.

4.3 In-Flight Field Measurements

During the field test, the UAS was deployed for airborne measurements, providing a real-world test scenario without the constraints of a controlled test-bed or inconsistent RTK-GPS signals. The mission involved flying an 80-meter arc, and with RTK-GPS fixed, measurements were conducted in three flights, two forward flights and one backward flight. The results are shown in Figure 4.4.

The co-polar results demonstrate remarkable consistency, not only matching the chamber control patterns but also showing excellent overlap between flights, including the nulls and side-lobes. In contrast, the cross-polar isolation results exhibit consistency within

flights in the same direction but differ from flights in the opposite direction. This was the focus of this test, to find operational errors and inconsistency caused during flight.

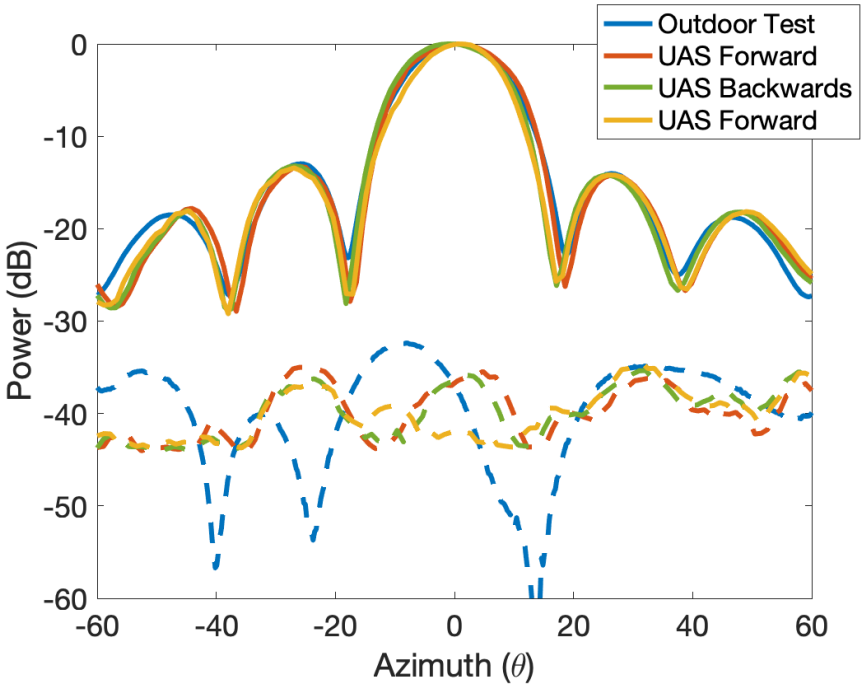

Figure 4.4: The far-field, H-plane, co-polar and cross-polar radiation patterns of the AUT as measured with the RF system in the anechoic chamber, compared with the near-nield patterns. The RF-System co-polar remains identical when measuring standalone or integrated into the UAS but there is a 4 dB increase in the cross-polar when integrated into the UAS.

Although, the cross-polar values are lower than those observed in the outdoor test which can be attributed to the antenna under test facing directly upwards which if a difference experimental setup and reduces ground reflections and multi-path, creating more ideal measurement conditions. The UAS being in flight also enables RTK-fixed lock, dramatically improving the positioning and tracking which also contribute to these results. Overall, the cross-polar values during the field test remain below -35 dB, indicating excellent performance. All systems were functional and real-time data was received on the ground station reliably as well as the high resolution data stored on the UAS was retrieved successfully.

4.4 Summary

Although the system was tested on a smaller phased array antenna model instead of an actual calibrated phased array radar system, the results are much better than expected for a UAS based RX measurements, as they are more susceptible to reflections from the UAS. There is great repeatability in the co-polar and cross-polar levels as low as -36 dB. The AUT was only rated until -42 dB in cross-polar, which further degraded to -33 dB in the outdoor hover test due to ground reflections. The actual spherical flight test yielded a much better results as a cross-polar of -36 dB was measured.

As the UAS-mounted RX measurements successfully achieve lower cross-polar levels than the outdoor hover test, this system takes the UAS-based calibration systems a setup closer to a fully airborne calibration system for radars. With further improvements to the AUT, the system is capable of obtaining measurements that can be applied to radar calibration.

Chapter 5

Epilogue

5.1 Conclusion

A study of the recent advancements in unmanned aerial system applications for radar and antenna characterization over the past decades is provided. The role of these technological developments in the rise of the UAS as a capable platform for reliable and accurate antenna pattern measurements is highlighted. Furthermore, limitations of existing UAS-based measurement system are identified, such as their reliance on predominantly large and ground-based stations and equipment, limited scanning capabilities and overall simple designs. Based on these limitations, the need for the development of a new, lightweight, and self-contained RF font-end system custom design for UAS-based airborne application in phased array antenna and radar characterization is emphasised and proposed.

The proposed RF system, built around a software-defined radio (SDR) technology, successfully addresses the limitations of previous systems. This new system is completely self-contained, small, low power, and lightweight. It is designed to receive power data from a probe through an SDR, process the data on an onboard computer, and transmit it to the UAS for storage. Furthermore, the UAS is well integrated equipped to communicate send real-time visualization data to the ground station through a custom Mavlink message. The system also incorporates the capability to switch polarization and between RX and TX

in real time, eliminating the need for mid-flight configuration changes, which can now be remotely controlled from the ground.

To validate the effectiveness of the proposed RF system, a series of experimental setups were devised. Measurements were conducted in a near-field chamber, a far-field chamber, outdoor environments, and finally, an in-flight test was performed. The obtained results from these setups have demonstrated the capability and reliability of the new RF system for radar and antenna characterization. While variations in results were observed across different setups, the final flight test yielded exceptional performance, achieving a cross-polarization isolation measurement of under -35 dB while simultaneously measuring co-polar and cross-polar patterns.

These findings have significant implications for the field of UAS-based radar and antenna characterization. The development of a lightweight and integrated RF system opens up new possibilities for conducting measurements with enhanced mobility, flexibility, and convenience. The ability to switch polarization and operate in real time provides greater efficiency and accuracy in data collection. Moreover, the real-time visualization capabilities enable researchers to monitor measurements and make any adjustments to the experiment in real time, further enhancing the usability and effectiveness of the system.

The successful design, development, and implementation of the proposed RF system have met the initial objectives of this paper. The system has proven to be reliable and capable of achieving high-quality measurements in a variety of environments. The advancements presented in this paper contribute to the growing body of research in UAS-based measurement systems and address the need for more compact and versatile solutions. It is expected that these developments will have a significant impact on the field, enabling further progress in radar and antenna characterization using UAS platforms.

In conclusion, this paper establishes the potential of UAS in radar and antenna characterization, showcases the development of a new SDR-based RF system, presents the results

of comprehensive experimental setups, and successfully achieves the initial objectives. The future prospects for UAS-based measurements are promising, and further research and advancements in this area will continue to shape the field of radar and antenna characterization.

5.2 Future Work

For future work, one of the main objectives would be to expand the capabilities of the system to measure actual radar systems. Currently, the system is designed for S-band systems which can be expanded for wider range of frequencies to adapt the system to work with both S- and X-band radars would allow for practical radar measurements and provide valuable insights into their performance.

For Chapter 1, using a more modern, reliable, and efficient drone could enhance the overall performance of the system. Upgrading to a newer drone model with advanced features, reduced weight, and extended flight time would minimize drone size and potential reflections, improving the accuracy of measurements. Additionally, advancements in battery technology could provide longer flight duration and increased power thresholds, resulting in improved RF performance. Another area for improvement is the gimbal system. While the current gimbal used in the experiments was effective, there are better gimbal options available. However, due to limited support and software, working with these advanced gimbals can be challenging. Devoting time and resources to developing dedicated software for these gimbals would enhance measurement accuracy and stability. Similarly, exploring new Software-Defined Radio (SDR) technologies could significantly improve system performance. The current SDR performed well for continuous waveform but faced limitations when used for pulse measurements. Upgrading to the latest SDR technologies with improved channel isolation and performance would enhance the system's capabilities.

The system's ability to simultaneously measure co-polar and cross-polar signals presents an opportunity for further research. By employing this capability, radar measurements can be conducted in grids and interpolated in post processing, this would enable the creation of 3D radiation beams and enhancing our understanding of radar antenna.

In Chapter 3, the AUT used was a phased array antenna, and the absence of an actual functioning radar limited the measurement possibilities. Replicating the measurements on a fully operational radar system, especially in the S-band, would yield more accurate and comprehensive results. Moreover, developing more in-depth protocols for UAS operations would be beneficial. These protocols would not only enhance researchers' awareness of UAS limitations and safety considerations but also ensure reliable and consistent performance during measurements.

References

[1] R. D. Palmer, M. B. Yeary, D. Schvartzman, J. L. Salazar-Cerreno, C. Fulton, M. McCord, B. Cheong, D. Bodine, P. Kirstetter, H. H. Sigmarsson, T.-Y. Yu, D. Zrnić, R. Kelley, J. Meier, and M. Herndon, "Horus—a fully digital polarimetric phased array radar for next-generation weather observations," *IEEE Transactions on Radar Systems*, vol. 1, pp. 96–117, 2023.

[2] R. J. Mailloux, *Phased array antenna handbook*. Artech house, 2017.

[3] C. J. Fulton, "Digital array radar calibration and performance monitoring techniques for direct conversion and dual polarization architectures," Ph.D. dissertation, Purdue University, 2011.

[4] E. E. A. S. Committee, *IEEE standard test procedures for antennas*. Institute of Electrical & Electronics Engineers (IEEE), 1979, vol. 149, no. 1979.

[5] J. S. Hollis, T. Lyon, and L. Clayton, *Microwave antenna measurements*. Scientific-Atlanta, 1970.

[6] S. T. P. Duthoit, *UAV-Based In Situ Antenna Characterization: Analysis and Design Requirements*. Master's Thesis, 2018.

[7] C. A. Balanis, *Antenna Theory: Analysis and Design*. Wiley-Interscience, 2005.

[8] D. J. Wasielewski, I. R. Ivic, and J. R. Mendoza, "Calibration of a dual-polarization planar phased-array radar using a far-field tower," in *99th American Meteorological Society Annual Meeting*. AMS, 2019.

[9] J. Steele, "Measurement of antenna radiation patterns using a tethered balloon," *IEEE Transactions on Antennas and Propagation*, vol. 13, no. 1, pp. 179–180, 1965.

[10] J.-E. Lejerkrans and F. Enquist, "Field strength measurement and antenna radiation pattern plotting using heli-borne equipment," in *1988 International Broadcasting Convention, IBC 1988*. IET, 1988, pp. 137–142.

[11] R. Manton and K. Beeke, "HF antenna radiation patterns over real terrain," in *1988 International Broadcasting Convention, IBC 1988*. IET, 1988, pp. 143–147.

[12] G. Virone, A. M. Lingua, M. Piras, A. Cina, F. Perini, J. Monari, F. Paonessa, O. A. Peverini, G. Addamo, and R. Tascone, "Antenna pattern verification system based on a micro unmanned aerial vehicle (UAV)," *IEEE Antennas and Wireless Propagation Letters*, vol. 13, pp. 169–172, 2014.

[13] G. Virone, F. Paonessa, O. A. Peverini, G. Addamo, R. Orta, R. Tascone, A. Lingua, M. Piras, P. Bolli, G. Pupillo *et al.*, "Antenna pattern measurement with UAVs: Modeling of the test source," in *2016 10th European Conference on Antennas and Propagation (EuCAP)*. IEEE, 2016, pp. 1–3.

[14] F. Paonessa, G. Virone, P. Bolli, G. Pupillo, J. Monari, F. Perini, A. Mattana, G. Naldi, M. Poloni, M. Schiaffino *et al.*, "The UAV-based test source as an end-to-end verification tool for aperture arrays," in *2016 International Conference on Electromagnetics in Advanced Applications (ICEAA)*. IEEE, 2016, pp. 886–889.

[15] M. García-Fernández, Y. Á. López, A. Arboleya, B. González-Valdés, Y. Rodríguez-Vaqueiro, M. E. D. C. Gómez, and F. L.-H. Andrés, "Antenna diagnostics and characterization using unmanned aerial vehicles," *IEEE Access*, vol. 5, pp. 23 563–23 575, 2017.

[16] G. Pupillo, G. Naldi, G. Bianchi, A. Mattana, J. Monari, F. Perini, M. Poloni, M. Schiaffino, P. Bolli, A. Lingua *et al.*, "Medicina array demonstrator: calibration and radiation pattern characterization using a UAV-mounted radio-frequency source," *Experimental Astronomy*, vol. 39, no. 2, pp. 405–421, 2015.

[17] J. L. Salazar, A. Umeyama, S. Duthoit, and C. Fulton, "UAS-based antenna pattern measurements and radar characterization," in *2018 IEEE Conference on Antenna Measurements & Applications (CAMA)*. IEEE, 2018, pp. 1–4.

[18] A. Y. Umeyama, J. L. Salazar-Cerreño, B. M. Wolf, and C. J. Fulton, "Recent development in UAV-based antenna pattern characterization for weather radars," in *2019 IEEE Conference on Antenna Measurements & Applications (CAMA)*. IEEE, 2019, pp. 199–202.

[19] A. Y. Umeyama, "Unmanned aerial vehicle-based far-field antenna characterization system for polarimetric weather radars," *University of Oklahoma*, 2020.

[20] A. Y. Segales, C. F. J. L. Salazar-Cerreno, and R. Palmer, "UAV-based antenna measurements for polarimetric weather radars: Probe analysis," *IEEE Access*, vol. 8, pp. 191 862–191 874, 2020.

[21] Rx-Block, "Light mechanics with much stronger motors," pp. fig2_355 196 740, https://www.jfwindustries.com/product/50s–1361–xx–sma–electro–mechanical–switch/, https://www.mvg–world.com/en/products/antennas/measurement–probes–and–feeds/open–boundary–quad–ridge–horns, https://www.fabtolab.com/radio–telemetry–apm, https://www.freepik.com/free–photos–vectors/laptop–png, 2023.

[22] H. Infinity-MR-PRO, “Light mechanics with much stronger motors,” pp. https://hdairstudio.com/infinity–mr–pro/, 2023.

[23] R. n. Getz, “Adalm-pluto detailed specifications. adalm-pluto detailed specifications [analog devices wiki],” pp. July 3, 2023, https://wiki.analog.com/university/tools/pluto/devs/specs.